

# Multi-instrument observations of various ionospheric disturbances caused by the 6 February 2023 Turkey earthquake

Haris Haralambous<sup>1</sup>, Marco Guerra<sup>2,3</sup>, Jaroslav Chum<sup>4</sup>, Tobias G. W. Verhulst<sup>5</sup>, Veronika Barta<sup>6</sup>, David Altadill<sup>7</sup>, Claudio Cesaroni<sup>2</sup>, Ivan Galkin<sup>8</sup>, Kiszely Márta<sup>9</sup>, Jens Mielich<sup>10</sup>, Daniel Kouba<sup>4</sup>, Dalia Buresova<sup>4</sup>, Antoni Segarra<sup>7</sup>, Luca Spogli<sup>2,11</sup>, Jan Ruzs<sup>4</sup>, Jan Zedník<sup>12</sup>

<sup>1</sup> Frederick University, School of Engineering, Nicosia, Cyprus

<sup>2</sup> Istituto Nazionale di Geofisica e Vulcanologia, Rome, Italy

<sup>3</sup> Sapienza Università di Roma, Rome, Italy

<sup>4</sup> Institute of Atmospheric Physics, Czech Academy of Sciences, Prague, Czech Republic

<sup>5</sup> Royal Meteorological institute of Belgium & Solar Terrestrial Centre of Excellence, Brussels, Belgium

<sup>6</sup> Institute of Earth Physics and Space Science, Sopron, Hungary

<sup>7</sup> Observatori de l'Ebre, Univ. Ramon Llull – CSIC, 43520 Roquetes, Spain

<sup>8</sup> University of Massachusetts Lowell, Space Science Laboratory, Lowell, United States of America

<sup>9</sup> Kövesligethy Radó Seismological Observatory, Institute of Earth Physics and Space Science, Budapest, Hungary

<sup>10</sup> Leibniz-Institute of Atmospheric Physics, Kuehlungsborn, Germany

<sup>11</sup> SpaceEarth Technology, Rome, Italy

<sup>12</sup> Institute of Geophysics Czech Academy of Sciences, Prague, Czech Republic

\* Correspondence: [eng.hh@frederick.ac.cy](mailto:eng.hh@frederick.ac.cy)

**Abstract:** In this work, we investigate various types of ionospheric disturbances observed over Europe after the earthquake in Turkey on 6 February 2023. By combining observations from Doppler sounding systems, ionosondes, and GNSS receivers, we are able to discern different types of disturbances, propagating with different velocities and through different mechanisms. We can detect the co-seismic disturbances produced in the ionosphere close to the epicenter, as well the ionospheric signatures of acoustic waves propagating as a consequence of propagating seismic waves.

**Keywords:** Earthquake; Total Electron Content; TID; infrasound; ionosonde; CDSS

## 44 1. Introduction

45

46 On 6 February 2023, two earthquakes with magnitude  $M_w > 7$  occurred in Turkey. The first  
47 shock was recorded at 01:17 UT with a magnitude of 7.8, while the second shock at 10:24 UT  
48 with  $M_w = 7.7$  (Çetin et al., 2023; Dal Zilio & Ampuero, 2023; US Geological Survey, 2023).  
49 These primary shocks were followed by many aftershocks with magnitude lower than 7. Both  
50 major earthquakes happened in the region of the East Anatolian Fault, with the epicenters  
51 separated by about 95 km. The first event was located at  $37.20^\circ\text{N}$ ,  $37.13^\circ\text{E}$ , and the second at  
52  $38.05^\circ\text{N}$ ,  $37.25^\circ\text{E}$ ; both events took place at a depth of around 10 km (International  
53 Seismological Centre, 2023; Bondár & Storchak, 2011).

54 The work of Leonard & Barnes (1965) and Davies & Baker (1965) concerning the great Alaskan  
55 earthquake of 1964, has already demonstrated that major earthquakes can cause disturbances in  
56 the ionosphere. Since then, it has been established that these ionospheric disturbances are  
57 manifested as different types of earthquake induced travelling ionospheric disturbances (TIDs),  
58 propagating through different mechanisms (Astafyeva, 2019; Meng et al., 2019).

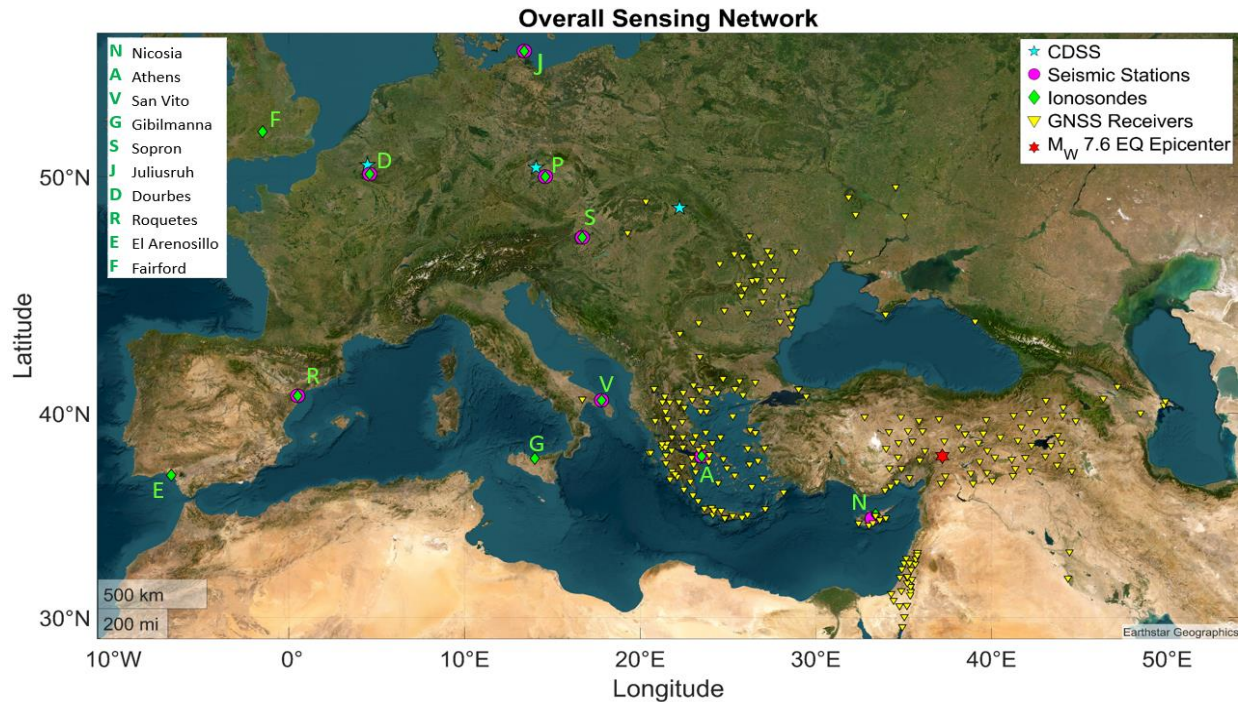
59 Co-seismic ionospheric disturbances are generated by waves travelling vertically up to the upper  
60 atmosphere in the vicinity of the epicenter (Afraimovich et al., 2001, Astafyeva & Afraimovich,  
61 2006, 2019). As shown by Rolland et al., (2013) through model results, these vertically  
62 propagating acoustic waves are accelerated and deflected horizontally due to the variation of  
63 atmospheric parameters with altitude. As a result, such acoustic waves are detected as fast TIDs  
64 propagating radially outward from the epicenter. Co-seismic disturbances start travelling out  
65 from their origin at around 1000 m/s, the speed of sound at the height of the F layer, but have  
66 been observed to split at some distance from the epicenter into different modes travelling with  
67 velocities of about 600 and 3000 m/s (Astafyeva et al., 2009, Galvan et al., 2012).

68 On the other hand, seismic waves propagating out from the epicenter—in particular Rayleigh  
69 surface waves—can also generate acoustic-gravity waves propagating up to the ionosphere  
70 (Astafyeva et al., 2009, Rolland et al., 2011, Komjathi et al., 2016). These disturbances are  
71 expected to propagate at the speed of the Rayleigh waves, between 2000 and 5000 m/s, but with  
72 a delay of around ten minutes required for the vertical propagation of disturbances from the  
73 ground to ionospheric altitude (Lognonné et al., 2006; Astafyeva, 2019). Since seismic waves on  
74 the ground can reach long distances, this mechanism can produce disturbances in the ionosphere  
75 beyond the range where the shock-acoustic waves travelling through the ionosphere are  
76 attenuated (e.g., Maruyama et al., 2016a; 2016b)

77 Finally, there are acoustic-gravity waves travelling much slower, with velocities in the order of a  
78 few hundred meters per second (Astafyeva et al., 2009, Meng et al., 2019). Besides the various  
79 types of travelling disturbances, evidence of longer lasting impacts on the ionosphere,  
80 particularly close to the epicenter (Astafyeva, 2019, and references therein) has been reported.  
81 However, such effects are not considered here.

82 Earthquakes with  $M_w > 6.5$  are expected to generate co-seismic disturbances in the ionosphere  
83 (Perevalova et al., 2014). The amplitude of ionospheric disturbances and the distance from the  
84 source at which they can be detected are of course dependent on the magnitude of the event, see  
85 for instance Heki (2021). In addition to the earthquake magnitude, the depth and the focal  
86 mechanism (Astafyeva & Heki, 2009) are also decisive factors that affect the excitation and  
87 propagation of TIDs. On top of these primary earthquake attributes, additional factors such as  
88 atmospheric conditions (Rolland et al., 2011) and the orientation of the geomagnetic field  
89 (Astafyeva & Heki, 2009; Zettergren & Snively, 2019) also define the characteristics of possible

90 ionospheric disturbances based on the coupling between the movement of the ground surface and  
 91 the upper atmosphere.  
 92 Thus, a complex view of a superposition of different types of travelling ionospheric disturbances  
 93 is observed after an earthquake, which differs significantly from one event to another. Besides  
 94 different modes of TIDs, also ionospheric signatures of infrasound can be observed in the  
 95 aftermath of major earthquakes (Chum et al., 2012; 2018a; Laštovička & Chum, 2017).  
 96 Ionospheric disturbances, including those resulting from an earthquake, can be detected using  
 97 Doppler sounders (Liu et al., 2006; Chum et al., 2012), ionosondes (e.g., Maruyama, 2016a), or  
 98 GNSS receivers that can facilitate TEC estimation (Calais & Minster, 1995; Afraimovich et al.,  
 99 2001). This complementary view from observations from different instruments, is ideal for  
 100 detecting different disturbance types (Astafyeva, 2019; Meng et al., 2019). In the European  
 101 region, all these instruments are available in relatively dense observational networks (see Figure  
 102 1). Disturbances can be observed from a close proximity to the epicenter to distances over  
 103 3000 km, and therefore velocities can be calculated. The aim of this paper is to present an  
 104 integrated picture of the various modes of TIDs generated during this event, as observed by  
 105 different monitoring networks.  
 106



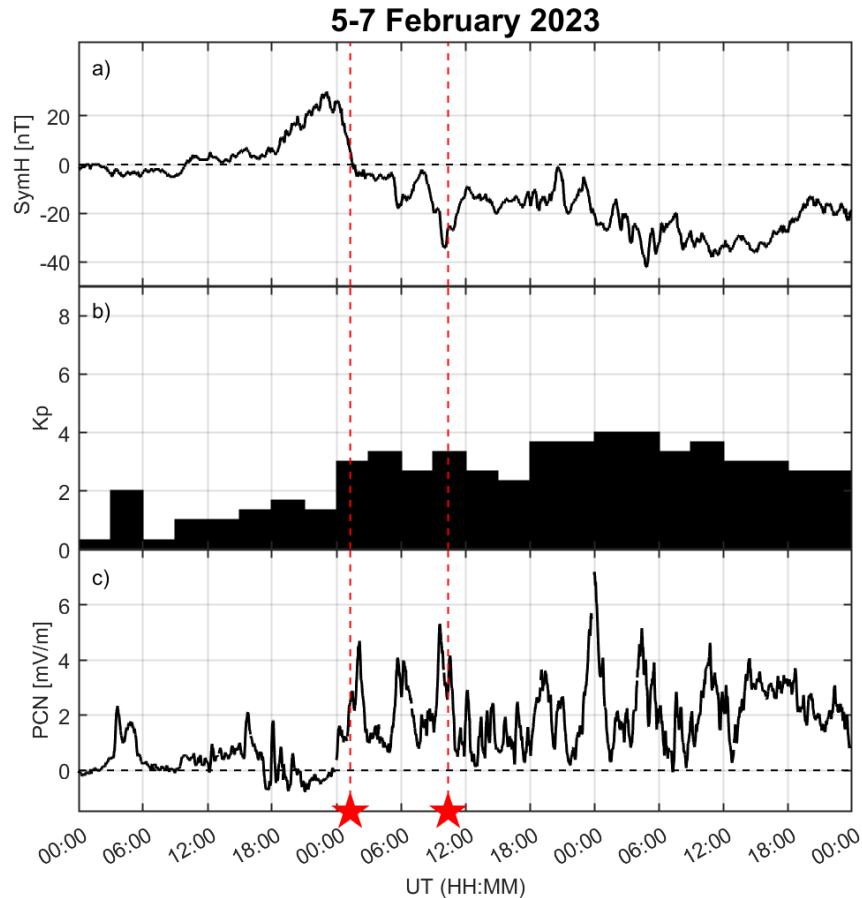
107  
 108 **Figure 1.** Map showing locations of instruments used for this study. The earthquake epicenter is also  
 109 shown (red asterisk).  
 110

## 111 2. Data and Methods

### 112 2.1 Geomagnetic conditions

113 The Turkey earthquakes took place during the ascending phase of the 25<sup>th</sup> solar cycle.

114



115  
 116 **Figure 2.** SymH (panel a), Kp (panel b) and Polar Cap North Index (panel c), in the period 5-7 February  
 117 2023. The red dashed lines and the corresponding stars indicate the time of the two main shocks (01:17  
 118 and 10:24 UT on 6 February 2023).  
 119

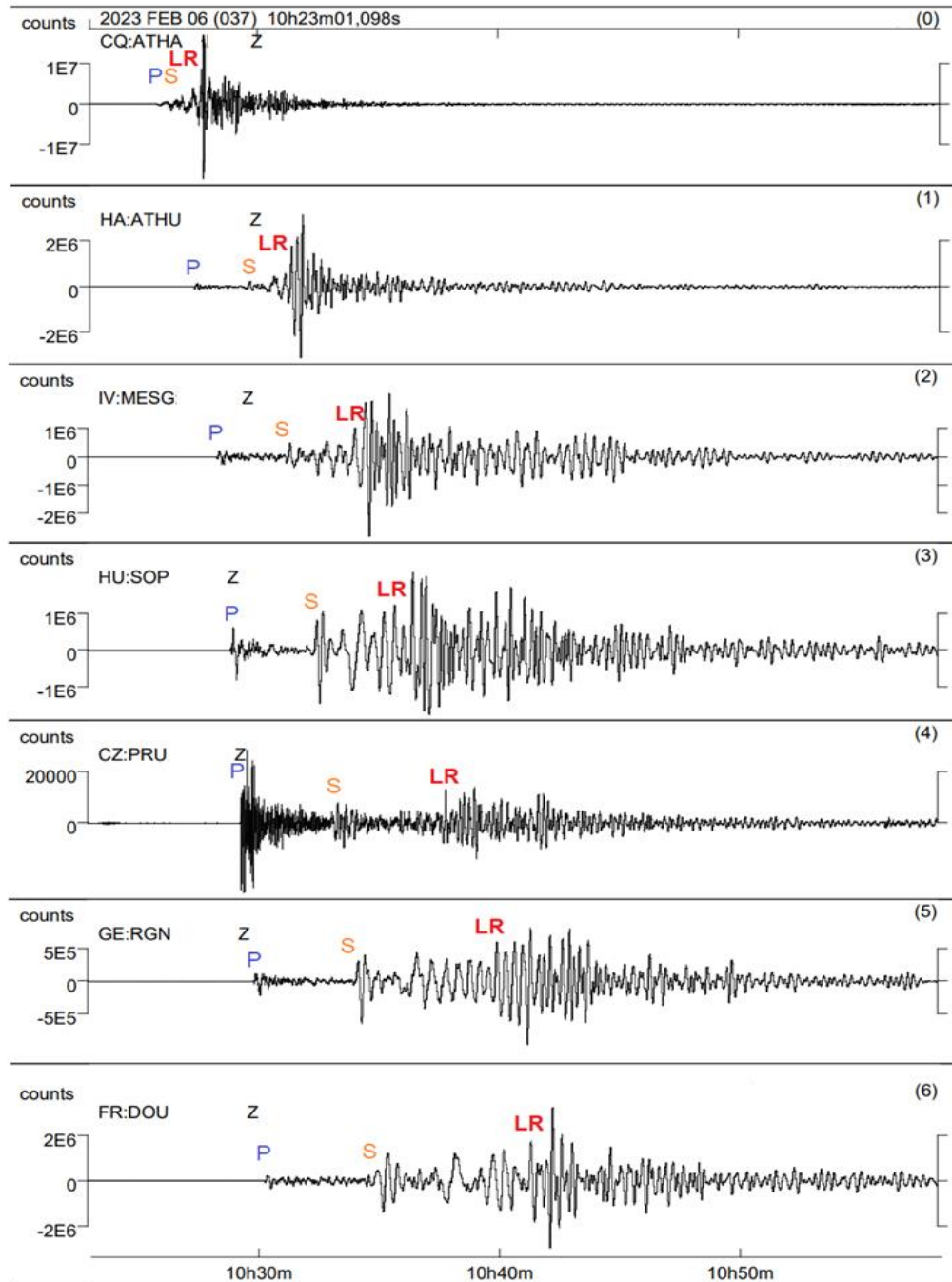
120 To quantify geomagnetic disturbances measured on the ground, the SymH (Li et al., 2011), Kp  
 121 (Kaurisiti et al., 2017) and Polar Cap North (PCN) index (Stauning, 2013) have been considered.  
 122 Figure 2 shows the time series of the respective indices in the period 5-7 February 2023, also  
 123 indicating the time of the two main shocks (01:17 and 10:24 UT on 6 February 2023) in red.  
 124 From the late evening of February 5, the solar wind speed increased, revealing the occurrence of  
 125 a high speed stream (HSS) linked to a coronal hole in the northern solar hemisphere  
 126 (Vanlommel, 2018). The solar wind speed slowly increased during 6 February and reached a  
 127 speed of 600 km/s on 7 February. In correspondence with the passage of such a HSS and under  
 128 favorable conditions of the Interplanetary Magnetic Field, geomagnetic disturbances covering  
 129 the period under consideration are found. As reported in Figure 2a-c, these disturbance maximize  
 130 in the early hours of 7 February (SymH= -42 nT, Kp=4, PCN=8.3). These solar driven  
 131 disturbances manifested in the ionosphere as spread-F, visible during the nighttime in the higher  
 132 latitude ionospheric observatories. In addition, the first main shock took place during a local  
 133 winter night, when background ionization is low. Conversely, during the daytime a positive  
 134 storm was observed with somewhat enhanced TEC values (Vanlommel, 2018). As a result of these  
 135 conditions, no clear indication of ionospheric disturbances were detected over Europe after the  
 136 first shock 01:17 UT, and the rest of this paper focuses on the second main shock at 10:24 UT.

139 **2.2 Seismic context**

140

141 The different types of seismic waves (body waves: primary P and secondary S, surface waves:  
142 Rayleigh waves LR and Love waves LQ) generated by the main shocks were identified at many  
143 seismic stations, some of which are located close to an ionosonde station (Figure 1). Figure 3  
144 shows the appearance of seismic waves at various seismic stations co-located with an ionosonde  
145 station after the Mw 7.7 earthquake ( $T_0 = 10:24:52$  UT). The velocity of the seismic surface  
146 waves can be calculated based on the arrival times of the waves and the ground distance of the  
147 seismic stations from the epicenter (Table 1). The seismic data is available in the European  
148 Integrated Data Archive (EIDA, Strollo et al. 2021). The amplitude of seismic waves registered  
149 at Nicosia (ATHA station) were so strong that they caused saturation of the instrument.  
150 Determination of Rayleigh wave packets at stations closer to the epicenter is not easy in the case  
151 of such a large earthquake. Two types of surface waves (Love and Rayleigh waves) arrive with a  
152 minor delay with respect to the S phase. Furthermore, local effects can modify the shape of the  
153 waves. We considered the propagation speed of the LR waves to identify the correct Rayleigh  
154 arrival time to the different stations during the manual selection.

155



156  
 157  
 158  
 159  
 160  
 161  
 162  
 163  
 164  
 165

**Figure 3.** Vertical seismic wave component (Z) recorded at different seismic stations (close to an ionosonde station in Europe) as generated by the earthquake at 10:24 (UT), in order of increasing distance from the epicenter. “Counts” in the y-axis is the raw number read off the physical instrument, ie. the voltage read from a sensor. For example, a “count” value of 3.27508E9 would indicate ground motion of 1 m/s — you can divide the count value by 3.27508E9 to convert into meters per second. However, this multiplier varies from station to station. P, S and Rayleigh wave (LR) indicate the corresponding wave type in the subplots.

Name	Code	Geographic Latitude [°N]	Geographic Longitude [°E]	Distance [km]	Arrival times [UT]		
					P waves	S waves	Rayleigh wave
Athalassa, Cyprus	ATHA	35.1	33.4	460	10:25:52	10:27:07	-
Athens, Greece	ATHU	37.9	23.8	1199	10:27:22	10:29:23	-
Mesagne, Italy	MESG	40.6	17.8	1691	10:28:25	10:31:17	10:32:02
Sopron, Hungary	SOP	47.7	16.6	1975	10:29:02	10:32:17	10:32:40
Průhonice, Czech R.	PRU	50.0	14.5	2232	10:29:25	10:33:09	10:34:17
Ruegen, Germany	RGN	54.5	13.3	2574	10:29:56	10:34:07	10:36:31
Dourbes, Belgium	DOU	50.1	4.6	2900	10:30:25	10:34:53	10:37:23

166  
167  
168  
169  
170

**Table 1.** List of seismic stations, which are situated close to a European ionosonde station, in order of increasing distance from the epicenter: name, code and attributes (latitude, longitude, and distance from epicenter in km) of the stations, and the arrival time of different waves at the stations.

### 171 2.3 Continuous Doppler Sounding Systems

172 The European network of Continuous Doppler Sounding Systems (CDSS) currently consists of  
173 the multi-point and multi-frequency system operating in the Czech Republic at frequencies of  
174 3.59, 4.65 and 7.04 MHz (Laštovička and Chum, 2017; Chum et al., 2021) and systems recently  
175 installed (at the end of 2022) in Belgium and Slovakia operating at frequencies of 4,59 and 3.59  
176 MHz, respectively. Data from the Belgian transmitter in Dourbes (50.099°N, 4.591°E) received  
177 in Uccle (50.798°N, 4.358°E), the Czech transmitter located in Dlouha Louka (50.648°N,  
178 13.656°E) received in Prague (50.041°N, 14.476°E), and the Slovak transmitter in Zahor  
179 (48.625°N, 22.205°E) received in Kolonica (48.935°N, 22.274°E), shown in Figure 1, were  
180 analysed in this paper. It should be noted that half distances between the transmitters and  
181 corresponding receivers are several times smaller than the reflection heights, so the zenith angle  
182  $\alpha$  of sounding radio waves is small and therefore  $\cos(\alpha) \approx 1$ . The surface horizontal distances of  
183 midpoints between the listed transmitter – receiver pairs in Belgium, the Czech Republic and  
184 Slovakia from the epicenter of the Turkey earthquake are about 2920, 2280 and 1700 km,  
185 respectively.

186 CDSS measure the Doppler shift that radio waves are subjected to, when reflected from the  
187 ionosphere due to the plasma motion and changes in electron density (Davies et al., 1962; Jacobs  
188 and Watanabe, 1966). CDSS have a relatively high time resolution (several seconds) due to the  
189 continuous sounding of harmonic radio waves of a specific frequency, but they do not provide  
190 any information about the reflection height, the region which contributes most to the observed  
191 Doppler shift (Chum et al., 2016a, 2018b). Therefore, it is useful to operate CDSS in the vicinity  
192 of an ionospheric sounder that can provide information on the CDSS sounding frequency  
193 reflection height, which is essential for a variety of studies (Chum et al., 2012; Chum et al.,  
194 2021). CDSS mainly detect medium scale travelling ionospheric disturbances (TID) or spread F  
195 (Chum et al., 2014; Chum et al., 2021), but they can also be used for the analysis of electric field  
196 that penetrates the ionosphere during geomagnetic storms (Kikuchi et al., 2021, 2022),  
197 infrasound generated by earthquakes (Artru et al., 2004; Chum et al., 2012, 2016a,b), typhoons  
198 and severe tropospheric weather (Georges, 1973; Chum et al., 2018a) or volcano eruptions

199 (Chum et al., 2023), ionospheric response to solar eclipses (Sindelarova et al., 2018; Liu et al.,  
 200 2019), solar flares (Chum et al., 2018b) etc.

201 It was shown by Watada et al. (2006) that the near surface pressure fluctuations and air  
 202 particle oscillation velocities  $w_0$  are determined by the vertical component of the velocity of  
 203 Earth surface motion,  $v_z$ . A high correlation between the waveforms of  $v_z$  for P and S seismic  
 204 waves and air particle oscillation velocities  $w$  in the ionosphere determined from Doppler shift  $f_D$   
 205 were shown in (Chum et al., 2012). The similarity of spectral content of  $v_z$  and  $w$  ( $f_D$ ) at large  
 206 distances from the earthquake epicenter was discussed in (Chum et al., 2016a, 2018a). The co-  
 207 seismic infrasound registered by CDSS during the earthquake under consideration was compared  
 208 with ground surface vertical velocities  $v_z$  measured by seismometers and observed time delays  
 209 between  $v_z$  and  $w$  ( $f_D$ ) were compared numerical simulation using ray tracing code described in  
 210 previous works (e.g., Chum et al., 2023). In addition, the values of  $w$  obtained from measured  
 211 Doppler shifts were compared with the amplitudes of  $w$  expected for infrasound propagating up  
 212 to the CDSS reflection heights assuming a linear theory of propagation and attenuation due to the  
 213 viscosity, thermal conductivity and rotational relaxation (Bass et al., 1984; Chum et al., 2012).  
 214 The air particle oscillation velocity  $w$  was estimated from the Doppler shift  $f_D$  using the  
 215 approximate formula (1) derived in (Chum et al., 2016a) for (quasi)vertical sounding and  
 216 (quasi)vertically propagating infrasound.

217

$$218 \quad w = -f_D \cdot \frac{c}{2f_0 \sin^2(I)} \cdot \frac{\frac{\partial N}{\partial z}}{\sqrt{(\frac{\partial N}{\partial z})^2 + (N \frac{2\pi f_{IS}}{c_s})^2}}, \quad (1)$$

219

220 where  $c$  is the speed of light,  $f_0$  is the sounding frequency,  $I$  is the inclination of geomagnetic  
 221 field,  $N$  is the electron density at the reflection height,  $\partial N/\partial z$  is the vertical gradient of electron  
 222 density at the reflection height estimated from the ionogram,  $f_{IS}$  is the infrasound frequency and  
 223  $c_s$  is the sound speed. The term  $N \cdot (2\pi f_{IS})/c_s$  results from the air and plasma compression due to  
 224 the infrasound waves. If  $\partial N/\partial z \gg N \cdot (2\pi f_{IS})/c_s$ , equation (1) reduces to (2)

225

$$226 \quad w = -f_D \cdot \frac{c}{2f_0 \sin^2(I)} \quad (2)$$

227

228 which is a relation that directly follows from the vertical plasma velocity  $w_p$ , computed from the  
 229 Doppler shift  $f_D$  by standard equation (3)

230

$$231 \quad w_p = -f_D \cdot \frac{c}{2f_0}, \quad (3)$$

232

233 assuming that (quasi)vertically propagating radio waves reflect from the magnetized plasma,  
 234 where electrons freely move only along magnetic field lines and are forced by vertically  
 235 oscillating air.

236

237

238

239

240

241

242 **2.4 Ionograms**

243 An ionospheric earthquake-related signature established as a deformation on ionograms is the  
244 multiple-cusp signature (“MCS”) which appears as additional cusps that can be attributed to  
245 electron density irregularities giving rise to stationary points of inflection in the vertical electron  
246 density profile as discussed by Maruyama, et al. (2011, 2012, 2014). This ionogram signature is  
247 shown in Figures 7 and 8 for several ionospheric stations and may be interpreted as an indication  
248 of the propagation of an acoustic wave as the separation of these points of inflection reflects the  
249 infrasound wavelength in the thermosphere. For this particular event all ionosondes considered  
250 were situated towards north-west with respect to the epicenter with the exception of the nearest  
251 ionosonde to the epicenter located at Nicosia which is positioned south-west with respect to the  
252 epicenter. All eleven ionosondes across Europe considered in this study along with their  
253 respective ionogram cadence are tabulated in Table 2 in accordance to their distance from the  
254 epicenter. Their location is also shown in Figure 1.  
255  
256

Station	URSI Code	Geographic latitude	Geographic longitude	Ionogram Cadence (Min)	Distance From Epicenter (km)
Nicosia	NI135	35.2°N	33.4°E	5.0	460
Athens	AT138	38.0°N	23.5°E	5.0	1199
San Vito	VT139	40.6°N	17.8°E	7.5	1691
Gibilmanna	GM037	37.9°N	14.0°E	15.0	2029
Sopron	SO148	47.6°N	16.7°E	5.0	1975
Prùhonice	PQO52	50.0°N	14.6°E	15.0	2232
Juliusruh	JR055	54.6°N	13.4°E	5.0	2574
Dourbes	DB049	50.1°N	4.6°E	5.0	2900
Roquetes	EB040	40.8°N	0.5°E	5.0	3146
Fairford	FF051	51.7°N	-1.5°E	7.5	3358
El Arenosillo	EA036	37.1°N	-6.7°E	5.0	3835

257  
258 **Table 2.** European ionosondes used in the study, arranged according to distance from the  
259 earthquake epicenter.

260

261 **2.5 GNSS derived TEC**

262

263 To investigate the ionospheric signatures in Total Electron Content (TEC) we used a collection  
264 of GNSS networks spanning different distances and azimuthal directions with respect to the  
265 epicenter (shown as yellow inverted triangles in Figure 1). Data from 1s and 30s RINEX files  
266 were used, with 1s as the preferred time resolution due to the relatively short period expected  
267 from co-seismic TID (Astafyeva, 2019). The GNSS stations used belong to many different  
268 institutions and networks, specifically INGV (Michelini et al., 2016), TUGASA-Aktif (Ouml et  
269 al., 2011), CYPOS (Danezis et al., 2019), NOA (Chousianitis et al., 2021), IGS (Dow et al.,  
270 2009), and EUREF (Torres et al., 2009). To extract TEC perturbations, we used the dual  
271 frequency geometry-free linear combination of carrier-phase measurements. The TEC along the  
272 satellite-receiver line of sight can be calculated starting from phase measurements as follows:

273

274

$$sTEC_{phase} = \frac{1}{40.308} \frac{f_1^2 f_2^2}{f_1^2 - f_2^2} (L_1 \lambda_1 - L_2 \lambda_2) \quad (4)$$

275

276

277

278

279

280

281

282

283

284

285

286

287

288

289

290

291

292

293

294

295

296

297

298

### 3. Observations and Discussion

299

300

301

#### 3.1 CDSS

302

303

304

305

306

307

308

309

310

311

312

313

314

315

316

317

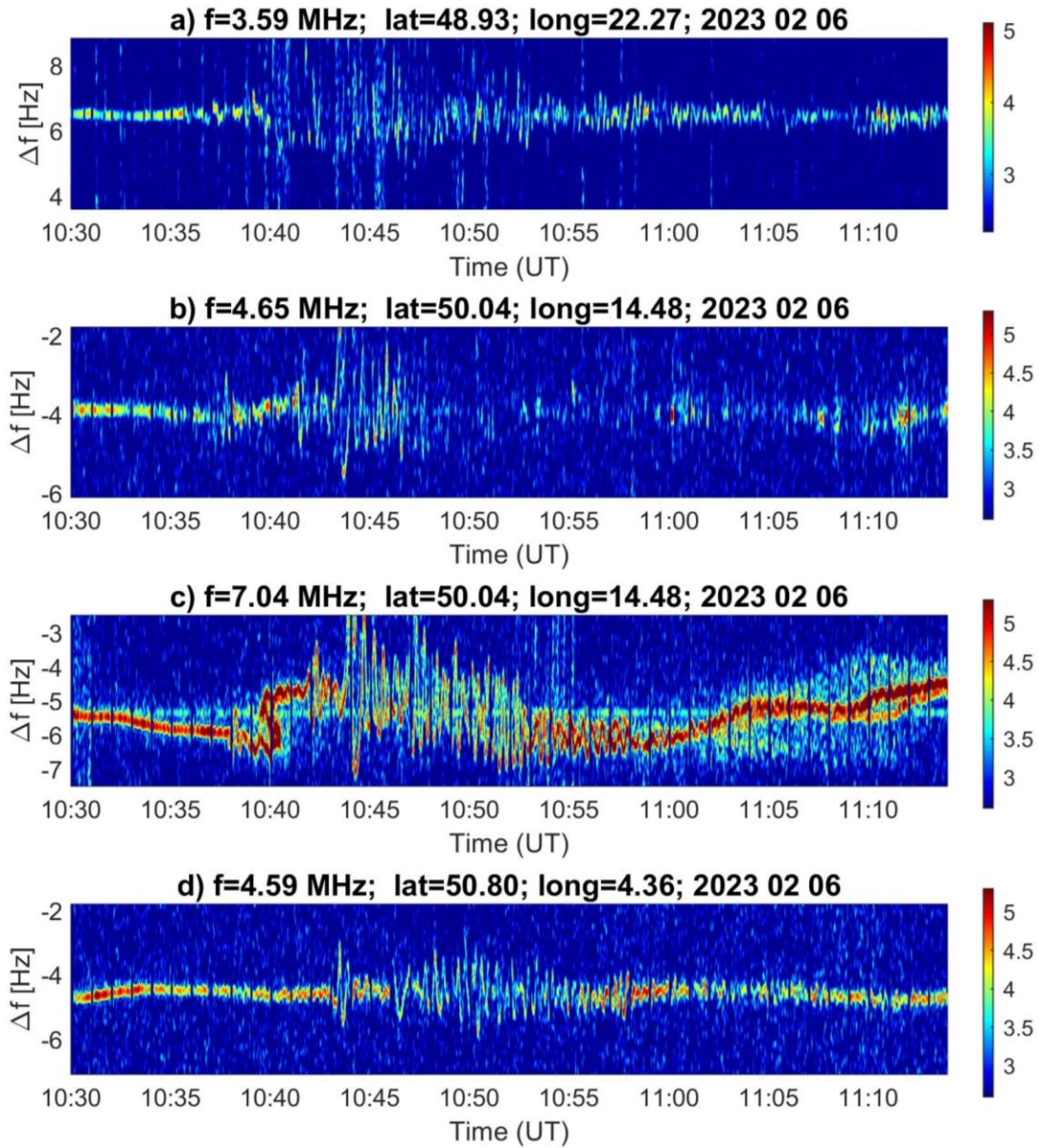
Figure 4 shows the Doppler shift spectrograms recorded by CDSS in Slovakia, the Czech Republic and Belgium after the M=7.7 Turkey earthquake on 6 February 2023. All four spectrograms show disturbances caused by infrasound waves. The Doppler shift fluctuations are not very clear in Slovakia, which prevents further analysis. However, Doppler shift time series could be obtained from maxima of spectral densities in the Doppler shift spectrograms recorded in the Czech Republic and Belgium and were used for further analysis.

Figure 5 displays the vertical component of the ground surface velocity  $v_z$  measured in Panská Ves, Czech Republic (plot a) and vertical plasma velocity  $w_p$  and air particle oscillation velocity  $w$  derived from the Doppler shift time series obtained from CDSS operating at  $f=4.65$  MHz and 7.04 MHz (plots b and c, respectively). The fluctuations of  $w_p$  ( $w$ ) in the Czech Republic derived from the 4.65 MHz signal are shorter than those derived from 7.04 MHz signal due to the low quality Doppler shift spectrogram after ~10:47 UT (Figure 4.b). The long-term variations, seen mainly in plots c in Figures 4 and 5 are caused by TIDs not related to the earthquake. On the other hand, the fast variations are due to the infrasound with a period about 20 s and clearly correspond to the variations of  $v_z$  shown in Figure 5.a. In particular, the similarity between  $v_z$  and

318  $w_p$  ( $w$ ) for the first pulse (around 10:29:40 UT in  $v_z$ ), which correspond to P seismic waves is  
319 remarkable. The corresponding signatures in the ionosphere recorded by the CDSS are delayed  
320 about 485 s for the 4.65 MHz sounding and about 515 s for the 7.04 MHz sounding. A clear  
321 similarity between  $v_z$  and  $w_p$  ( $w$ ) is also observed for the second pulse (around 10:33:32 UT in  $v_z$ )  
322 corresponding to S seismic waves. The S waves are then followed by Rayleigh waves of higher  
323 amplitude and by their corresponding ionospheric signatures. The bottom plots (d) and (e) show  
324 ground velocity  $v_z$  and the corresponding plasma velocities  $w_p$  and air particle oscillation  
325 velocities  $w$  estimated from CDSS observation in Belgium.

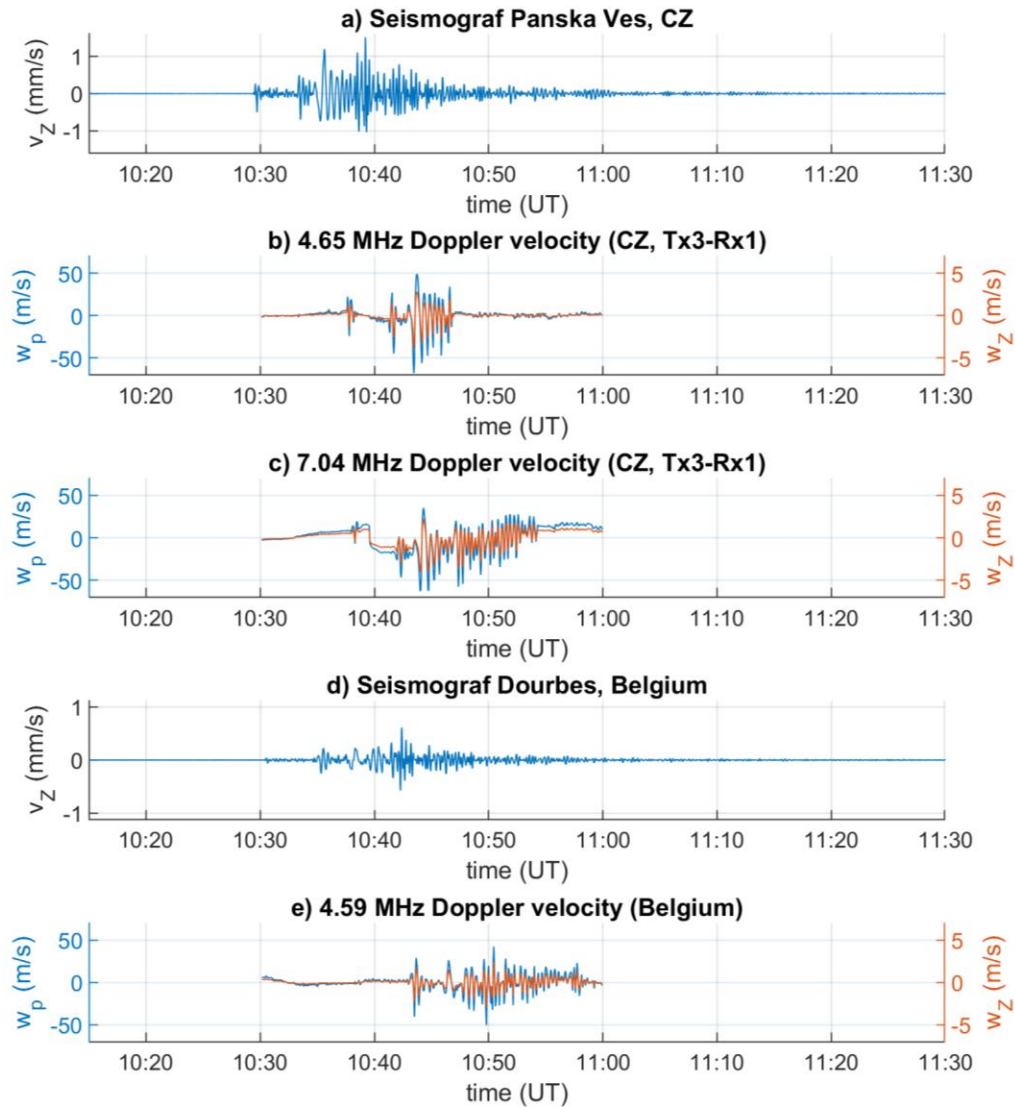
326  
327 Figure 6 shows the ray tracing simulation results for acoustic waves with a period of 20 s for a  
328 realistic atmosphere over the Czech Republic including the neutral horizontal winds obtained by  
329 HWM14 model (Drob et al., 2015) on 6 February 2023 at 10:45 UT. The ray tracing was  
330 initialized with zenith angles from  $2^\circ$  (red) to  $6^\circ$  (blue). This range covers the expected initial  
331 zenith angles  $\alpha_0$ , given by the ratio  $c_{SO}/c_G$ ,  $\sin \alpha_0 = c_{SO}/c_G$ , where  $c_{SO}$  is the near surface sound  
332 speed and  $c_G$  is the speed of seismic waves (Rolland et al., 2011; Chum et al., 2016a). The ray  
333 tracing extended up to an altitude of 300 km. The rays reach the altitudes of about 170 km and  
334 190 km for the observed time delays of 485 s and 515 s, respectively (Figure 6.c), which is  
335 consistent with CDSS reflection heights derived from ionograms measured by the nearby  
336 Digisonde at Průhonice. Figure 6.b shows the calculated infrasound attenuation along the ray  
337 trajectories, related to the initial, near surface infrasound amplitude. The attenuation is also  
338 plotted in an alternative way in Figure 6.d, which shows the ratio  $w/w_0$ , which is the ratio of air  
339 particle oscillation velocities  $w$  at a specific height to the velocities  $w_0$  ( $w_0=v_z$ ) near the ground  
340 surface. The solid line represents the unrealistic case of lossless propagation (no attenuation).

341  
342 The simulated ratio  $w/w_0$  can be compared with the measured values  $v_z$ ,  $w$  and  $w_p$  ( $w/v_z$  and  
343  $w_p/v_z$ ) presented in Figure 5 (note different scales for  $v_z$ ,  $w$  and  $w_p$ ). The measured ratio  $w_p/w_z$  is  
344 about 50 000 and the ratio  $w/w_z$  obtained using equation (1) is about 5000. It should be stressed  
345 that the ratio  $w_p/w_z$  and hence the ratio  $w/w_z$  calculated by equation (2) is higher than the  
346 theoretical limit (about 28 000 at the height of 170 km) for lossless propagation (solid line in  
347 Figure 6.d) and significantly larger than the estimated/modeled ratio (about 15000 at 170 km)  
348 considering the attenuation. From this, it follows that the compressional term in equation (1)  
349 cannot be neglected when deriving the air velocities from the measured Doppler shift  $f_D$ . It  
350 should be remembered that there is a large uncertainty in electron density gradient derived from  
351 ionograms ( $\sim 6 \cdot 10^6 \text{ m}^{-4}$  at 170 km and  $\sim 10^7 \text{ m}^{-4}$  at 190 km). This may be one of the reasons why  
352 the measured ratio, of approximately 5 000 according to equation (1), is lower than the modelled  
353 one ( $\sim 15000$  at 170 km and  $\sim 11000$  at 190 km). Another reason is the divergence of infrasound  
354 ray trajectories (geometrical factor) that is not taken into account in the simulation. The actual  
355 attenuation of wave energy is expected to be stronger due to the ray divergence than that shown  
356 in Figures 6.b and 6.d.



357

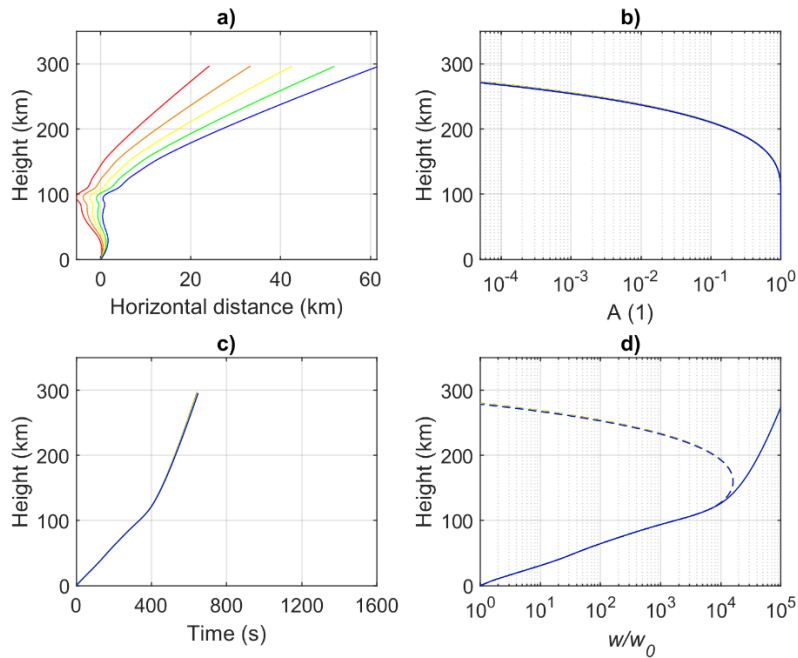
358 **Figure 4.** Doppler shift spectrogram recorded for selected sounding paths in (a) Slovakia, (b, c) Czech  
 359 Republic at  $f=4.65$  and  $7.04$  MHz, respectively (d) Belgium from 10:30 to 11:15 UT on 6 February 2023



360

361 **Figure 5.** (a) Vertical velocity  $v_z$  of ground surface in Panska Ves, Czech Republic, (b), (c) vertical  
 362 plasma velocity  $w_p$  (blue) and air particle velocity  $w_z$  (red) derived from measured Doppler shift by CDSS  
 363 in the Czech Republic at 4.65 and 7.04 MHz, respectively, (d) Vertical velocity  $v_z$  of ground surface in  
 364 Dourbes, Belgium and (e) vertical plasma velocity  $w_p$  (blue) and air particle velocity  $w_z$  (red) derived  
 365 from measured Doppler shift by CDSS in Belgium at 4.59 MHz.

366



367

368 **Figure 6.** Ray tracing results for the infrasound waves started from the surface with zenith angle 2° (red)  
 369 to 6° (blue). (a) Ray trajectories in vertical cross-section along the wave vector of seismic waves, (b)  
 370 Attenuation as a function of height (relative to initial value) calculated by the analytic model assuming the  
 371 wave period of 20 s, (c) Height as a function of time and (d) Ratio of air particle oscillation velocities  $w$  at  
 372 a specific height related to the near surface value  $w_0$ . Solid line represents the lossless propagation.  
 373

374 The CDSS did not detect any co-seismic disturbances related to M=7.8 earthquake that occurred  
 375 at night at 01:17:35 UT on the same day, 6 February 2023. The main reason besides the low  
 376 critical frequency  $foF2$  (only 3.59 MHz systems experienced reflection from the ionosphere) was  
 377 the high altitude of reflection (about 340 km). The simulation in Figure 6 clearly demonstrates  
 378 that infrasound waves of 20 s period are strongly attenuated above about 250 km and cannot be  
 379 detected by CDSS at such altitudes.

380 A similarity between the waveforms and spectra of the vertical ground surface velocity  $v_z$  and the  
 381 air particle oscillation velocity  $w$  determined from the observed Doppler shift  $f_D$  indicates that  
 382 the propagation of infrasound to the altitudes of observation in central Europe was linear. The  
 383 velocities  $v_z$  and hence the initial near surface perturbations  $w_0$  were not large enough to lead to  
 384 the nonlinear phenomena in the upper atmosphere that have been observed by CDSS in the  
 385 vicinity of strong earthquakes (Chum et al., 2016b; Chum et al., 2018a).  
 386

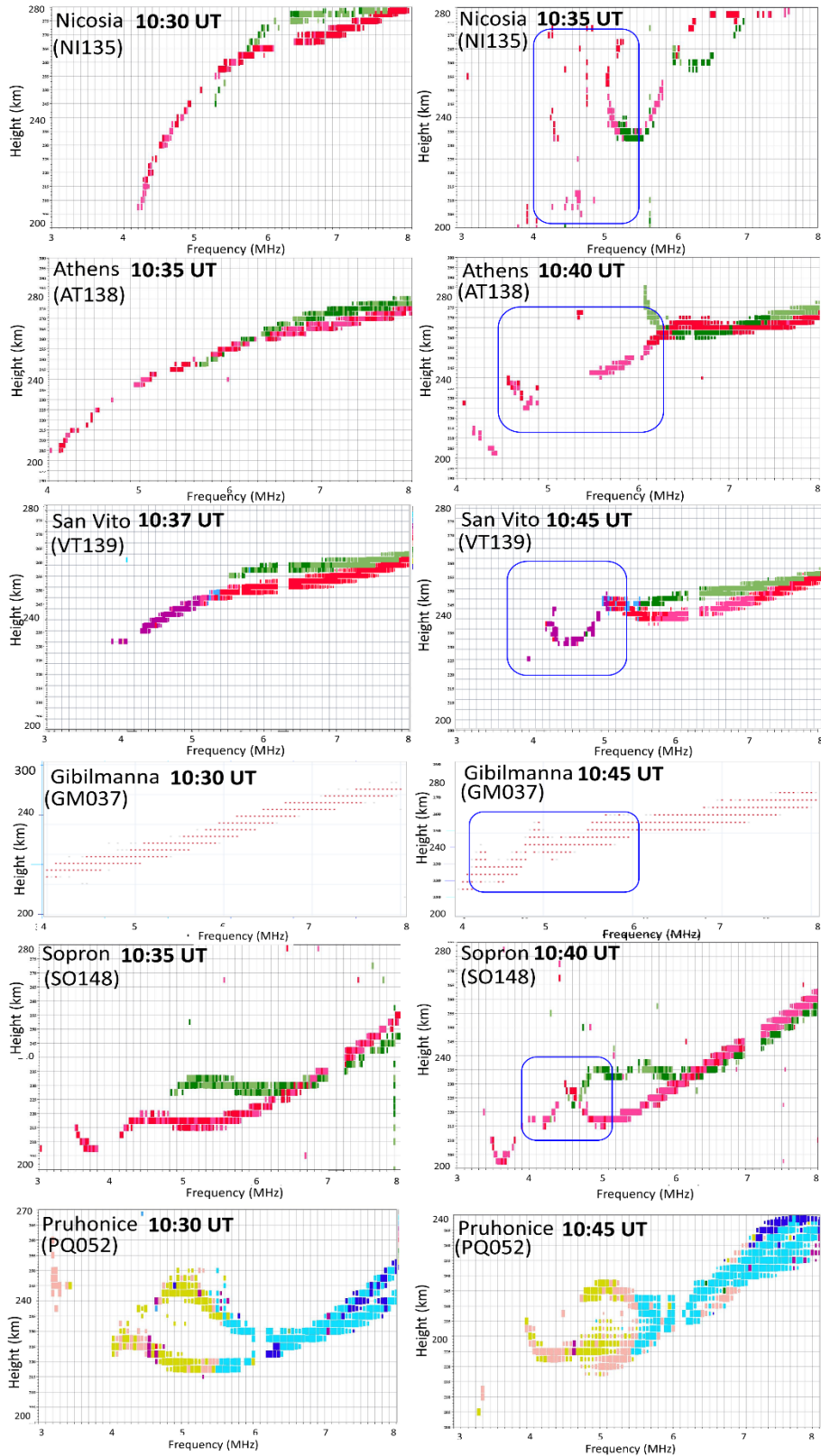
### 387 3.2 Ionograms

388 Each row in Figures 7 and 8 represents two ionograms for each of the ionosonde stations listed in  
 389 Table 2. Here the left column shows the latest seismic undisturbed ionogram. On the  
 390 corresponding ionograms for each of these stations a few minutes later (in the right column),  
 391 clear multi-cusp signatures are seen. The difference in the consecutive ionograms is particularly  
 392 evident at Nicosia, Athens, Gibilmanna, Juliusruh, Dourbes and Fairford. The disturbances  
 393 appear to be limited to the lower F region and the cusps are particularly sharp-edged in the case

394 of Juliusruh, Dourbes and Fairford. The cusps for San Vito, Sopron Roquetes and El Arenosillo  
395 are faint, but can still be identified when the traces are compared with the respective regular  
396 ionograms on the left.

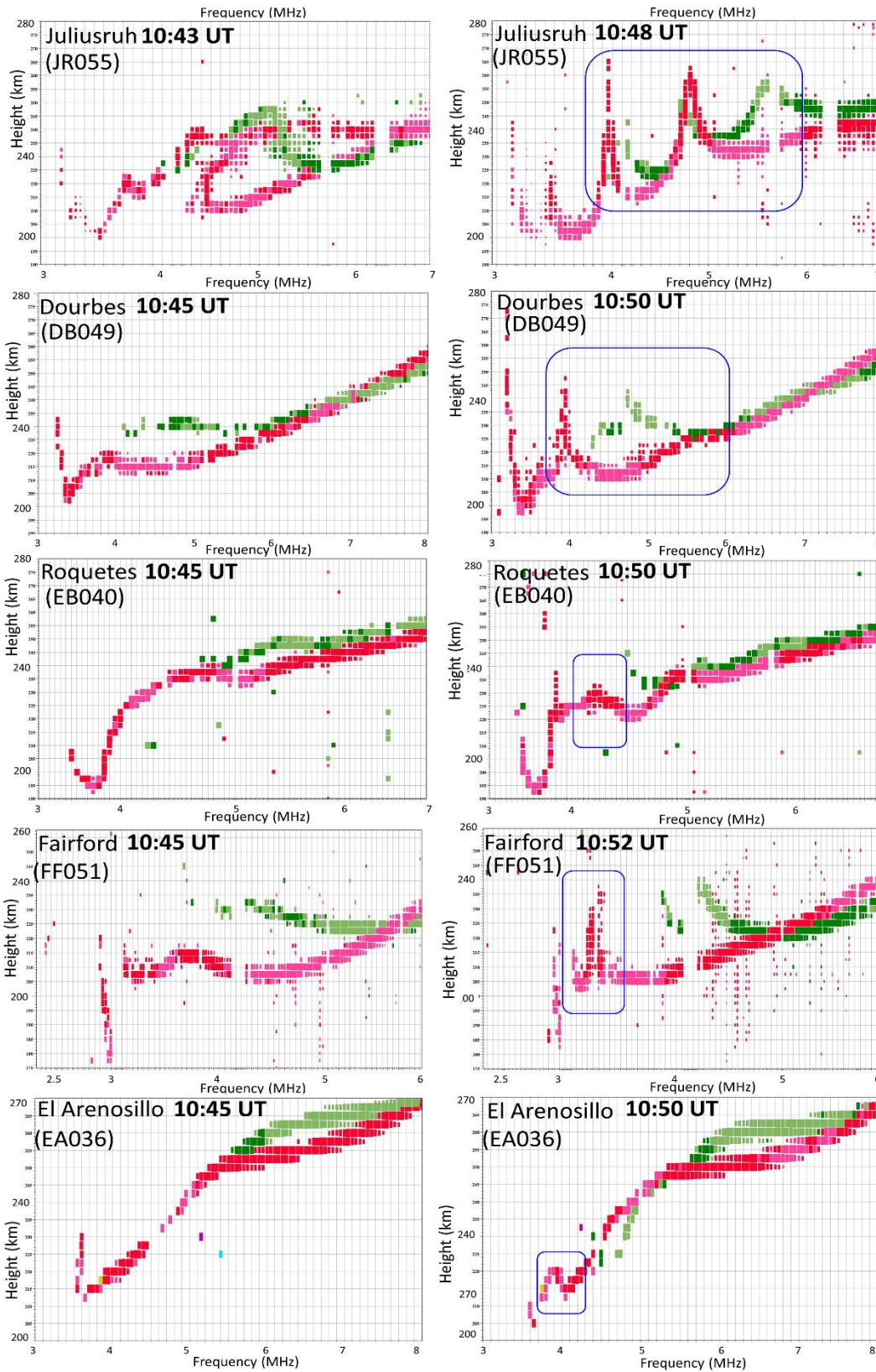
397

398 Considering ionograms from all ionosondes involved, we were able to detect clear “MCS” on  
399 ionograms from almost all stations (with the exception of Průhonice) after 10:35 UT at which the  
400 first signature appeared at the 10:35 UT Nicosia ionogram, which is in line with the arrival of the  
401 acoustic wave in the ionosphere at approximately 10 min after the seismic disturbances  
402 generated by the 10:24 UT shock (indicated with the vertical line) as indicated in Figure 9. The  
403 appearance of the Rayleigh and Love wave signature in the ionosphere is delayed because of the  
404 propagation time of the atmospheric waves from the ground into the ionosphere after the seismic  
405 disturbance has reached the ionosonde location. In fact, associated “MCS” can be identified in  
406 the subsequent ionograms on more distant stations (as ionograms from top to bottom in Figure 7  
407 and Figure 8 are ordered in accordance to their distance from the epicenter). Despite the fact that,  
408 ionograms at Průhonice (PQ052), due to some technical problem with the ionosonde at the time,  
409 do not contain correct polarization and direction of arrival information, the time of arrival of  
410 individual signals is, reliable. In other words – we can use the individual traces on the ionogram,  
411 but we cannot use the color codes of the signal for interpretation.



412  
413  
414

**Figure 7.** Successive ionograms at European stations (from top to bottom: Nicosia, Athens, San Vito, Gibilmanna, Sopron, Pruhonice) registering a clear multiple-cusp signature (“MCS”).

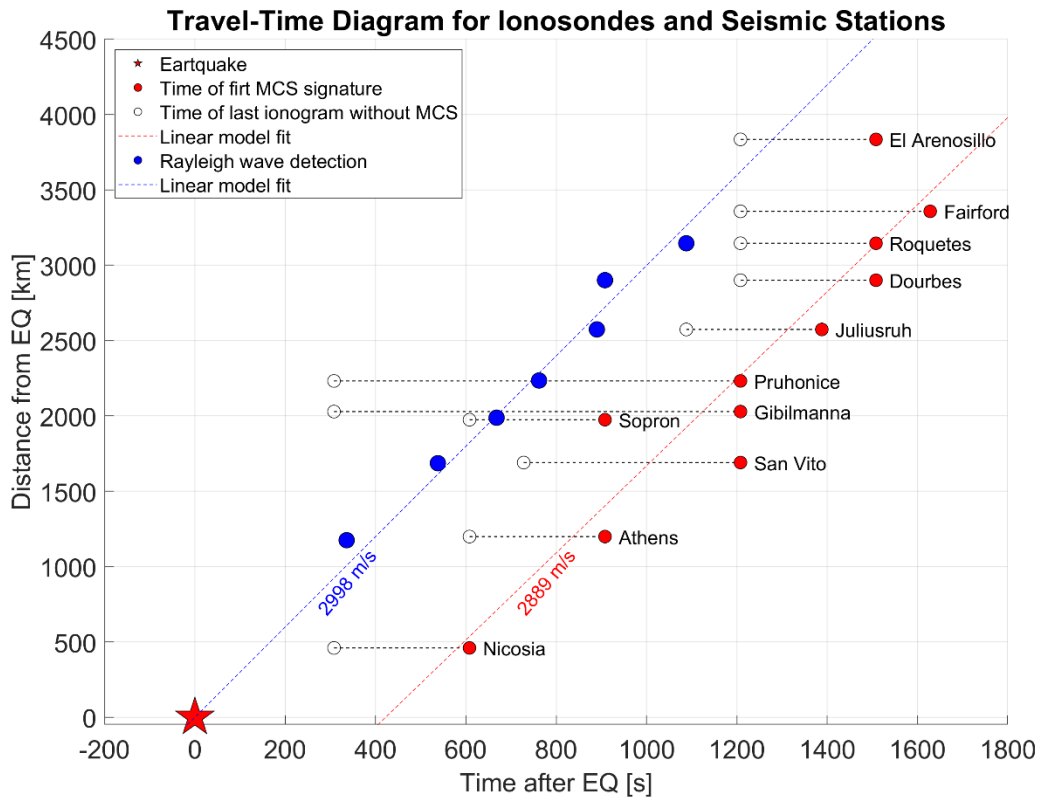


415  
416  
417

**Figure 8.** Successive ionograms at European stations (from top to bottom: Juliusruh, Dourbes, Roquetes, Fairford, El Arenosillo) registering a clear multiple-cusp signature (“MCS”).

418 Figure 9 shows the time (horizontal axis) of the first acquisition of an ionogram with a “MCS”  
 419 after the earthquake (red circle) with respect to the previous unaffected ionogram (white circle)  
 420 as well as the time of the main shock (10:24 UT) as indicated by the red star on the x axis.  
 421 Apparently we can draw a line through these points with a slope approximating the disturbance  
 422 propagation velocity but clearly there exists an ambiguity in defining this line as ionograms were  
 423 conducted at intervals of 5 to 15 min (Table 2). This ambiguity for each station is also reflected  
 424 on the time difference between red and white circles for each ionosonde (dotted line connecting  
 425 the two circles).

426 Compared to the high-temporal resolution provided by 1 s RINEX files in the GNSS analysis  
 427 shown in section 3.3 ionosondes are operated typically at a much lower temporal resolution  
 428 according to which they perform an ionogram measurement every 5-15 min intervals (as  
 429 indicated by consecutive ionograms from various European stations in Figures 7 and 8). During  
 430 such a time interval, an acoustic wave would cover a distance of more than 250 km under a  
 431 sound velocity assumption of 0.8 km/s. Unless the ionosonde operates on a campaign mode  
 432 where it performs an ionogram measurement every 30 s or 1 min it is not realistic to detect a  
 433 clear typical “MCS” on consecutive ionograms.  
 434



435  
 436 **Figure 9.** Travel-time diagram of co-seismic ionospheric disturbances causing “MCS”s at each station.  
 437

438 It is interesting to relate the time of arrival of the P, S and most importantly Rayleigh waves  
 439 according to the recordings of the seismic stations shown in Table 1 and the “MCS” appearance  
 440 on the ionograms indicated in Figures 7 and 8 considering the corresponding time ambiguity  
 441 based on the length of the line connecting each pair of white and red circles. For example  
 442 between Nicosia (nearest location to the epicenter as shown in Figure 1) and Athens, the  
 443 difference in the time of arrival in the P waves (10:25:52 at Nicosia and 10:27:22 at Athens) and

444 S waves (10:27:07 at Nicosia and 10:29:23 at Athens) is around 1-2 min (Rayleigh waves  
445 saturate the measurements at both seismic stations) whereas the “MCS” appears clearly on  
446 ionograms that are 5 min apart (10:35 at Nicosia and 10:35 at Athens). For the San Vito  
447 ionosonde we also have a definite estimation for the arrival of Rayleigh waves (10:32:02) the  
448 “MCS” appears on the 10:45 ionogram, which is beyond the 8-10 min delay relative to the  
449 Rayleigh waves arrival at the corresponding seismic station (MESG). However, we can identify  
450 that the “MCS” is not so evident for that specific case as compared to other stations (Nicosia,  
451 Athens Juliusruh and Dourbes). In particular, for Dourbes and Juliusruh the time difference in  
452 the Rayleigh wave arrival (10:36:31 at Juliusruh and 10:37:23 at Dourbes) is comparable to the  
453 time difference of a similar “MCS” appearance on the corresponding ionograms (10:48 at  
454 Juliusruh and 10:50 at Dourbes) which underlines the clarity of the “MCS” as a function of the  
455 time with respect to the ionogram measurement. This emphasizes the importance of the  
456 ambiguity depicted in Figure 9 with respect to the clear identification of “MCS” signatures at  
457 each station and the subsequent capability to determine the acoustic wave propagation in the  
458 ionosphere based on “MCS”. Although not included in Table 1 but considered in Figure 8, the  
459 arrival time of the Rayleigh wave in the Spanish seismic stations ERTA and CMAS was at  
460 approximately 10:43 UT. The ionospheric station Roquetes (EB040) in Spain recorded the  
461 “MCS” irregularities at 10:50 that compared to the arrival time of the Rayleigh wave identified  
462 on the nearest station seismogram at 10:43, this would result in an estimated travel time of the  
463 irregularity from ground to the ionosphere of about 7-8 minutes. The latter agrees well with the  
464 estimated travel time of about ten minutes required for the vertical propagation of disturbances  
465 from the ground to ionospheric altitude (Lognonné et al., 2006; Astafyeva, 2019). The small  
466 timing differences discussed above may be also attributed to the fact that ionograms provide  
467 information on a wide area of the sky over the measuring site and not over a single point but also  
468 on differences on the radiation patterns of transmitting and receiving antennas at the ionosonde  
469 sites. A notable conclusion that we can infer from Figure 9 stems out of the parallel red and blue  
470 lines indicating the ionospheric disturbance propagation and the corresponding driver of this  
471 disturbance which is the Rayleigh wave on the surface, respectively. If we accept that MCS  
472 signatures correspond to perturbations of the electron density profile around an altitude of 140  
473 km then the time shift of approximately 400 sec between the two (almost parallel blue and red  
474 lines) would infer a propagating upward velocity of this acoustic wave from the surface to the  
475 bottom of the F-layer at a velocity of 350 m/s.

476

### 477 3.3 GNSS

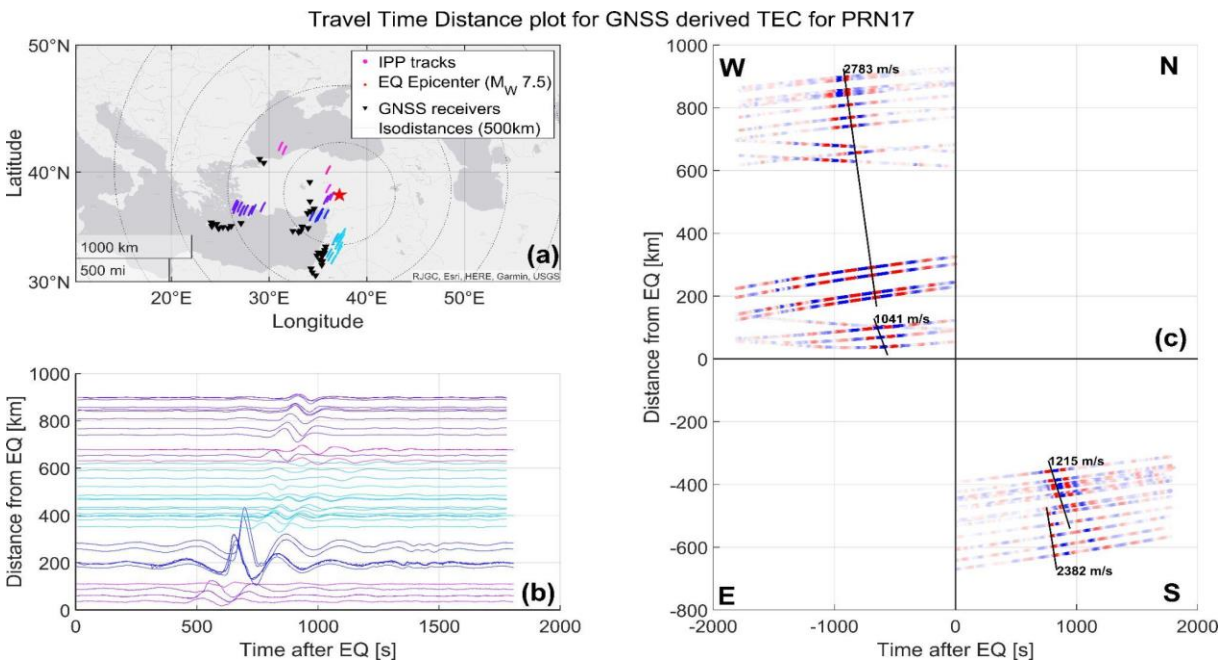
478

479 Once dTEC and the Ionospheric Pierce Points (IPPs) locations were calculated, we investigated  
480 the TID propagation in space through a travel-time diagram (TTD), a technique widely used to  
481 estimate velocities and time of arrival of co-seismic ionospheric waves at different locations  
482 (Astafyeva, 2019; Astafyeva et al., 2009). Moreover, we expanded the TTD further by dividing it  
483 into four sub-panels (Panel (c) of Figures 10, 11 and 12) each corresponding to different  
484 azimuthal ranges with respect to the earthquake epicenter. This modification facilitates the  
485 investigation of the anisotropies in the TID propagation and parameters, which is expected for  
486 co-seismic TIDs (Zettergren & Snively, 2019).

487

488 Figures 10, 11 and 12 show the aforementioned diagram for PRN17, PRN49 and PRN58  
489 respectively. Note that the satellites considered were not the only ones showing clear TID

490 signatures, but were chosen because they show the signature of both the shock acoustic wave  
 491 (Afraimovich et al., 2001; Astafyeva et al., 2009; Heki & Ping, 2005) and the Rayleigh wave induced  
 492 TID (Ducic et al., 2003; Rolland et al., 2011). The left Panels show the TTD itself, with the X and Y  
 493 axis representing the distance in time and space to the earthquake. Panels (a) show the spatial  
 494 distribution of IPPs, the epicenter location and its isodistances. Because of the TID being ion  
 495 density waves, the coupling of the neutral and ionized particles is maximal along magnetic field  
 496 lines since ion movement is mainly restricted along magnetic field lines (Bagiya et al., 2019;  
 497 Rolland et al., 2013). Thus, when investigating the different azimuthal features we need to take  
 498 into account that over Turkey the inclination and declination of magnetic field lines are  
 499 respectively around 55 and 5 degrees. Panels (b) show the TTD for the stations shown in Panels  
 500 (a). Note that the network used was denser than the one visible in Figure 1 (overall network  
 501 figure), because we decided to show only those station-satellite links with a clear signature.  
 502 Discarding such links also enabled the investigation of a possible preferred azimuth of  
 503 propagation by comparing the original spatial distribution and the one of Panels (a). Specifically,  
 504 we decided to plot only those arcs that showed a TID amplitude higher than 0.05 TECu.  
 505 (TECu). In addition, the IPP tracks are colored according to the initial arc azimuth to the  
 506 epicenter to highlight the different wave patterns. Finally, Panels (c) show a slightly different  
 507 TTD, where blue and red points correspond to negative and positive TEC perturbations.  
 508 Moreover, the TTD here was split into four different subpanels, each showing a different  
 509 azimuthal range with respect to the epicenter. Thus, the main difference between Panels (b) and  
 510 Panels (c) is that the distance shown in Panels (b) is the distance of the given IPP at the time of  
 511 maximum dTEC, while Panels (c) show its time evolution.  
 512



513 **Figure 10.** (a) Spatial distribution of IPPs and the epicenter location (b) Travel-time diagram for the  
 514 stations shown in (a) and (c) Travel-time diagram for different azimuth for PRN17.  
 515  
 516

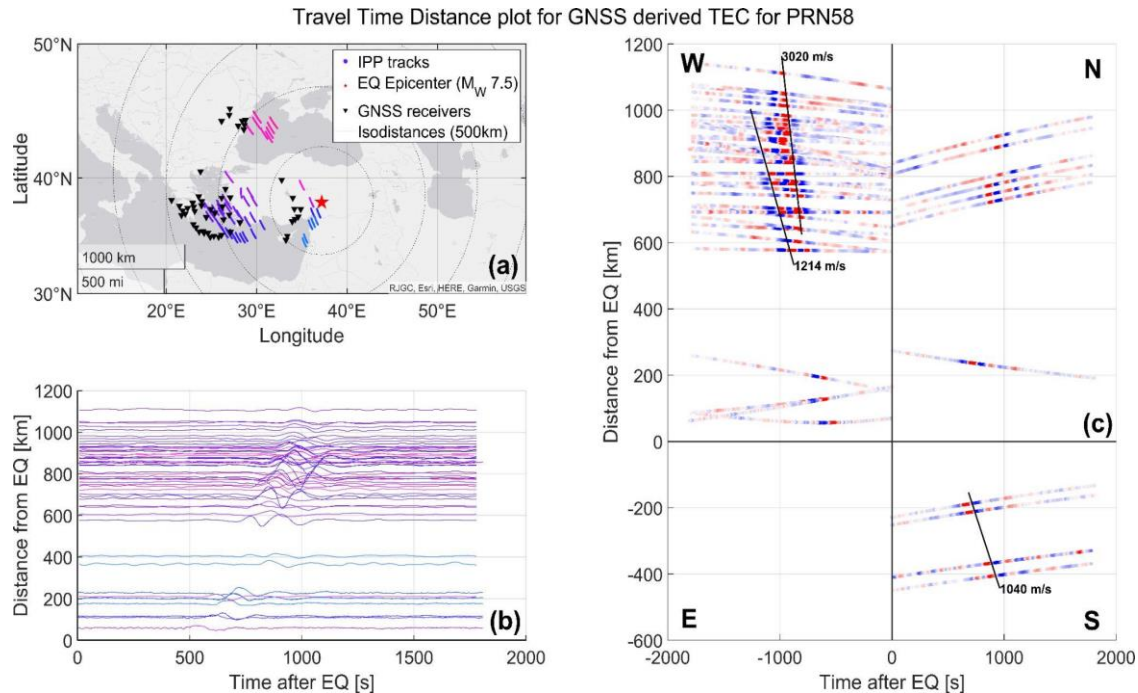


**Figure 11.** (a) Spatial distribution of IPPs and the epicenter location (b) Travel-time diagram for the stations shown in (a) and to be completed. (c) Travel-time diagram for different azimuth for PRN58.

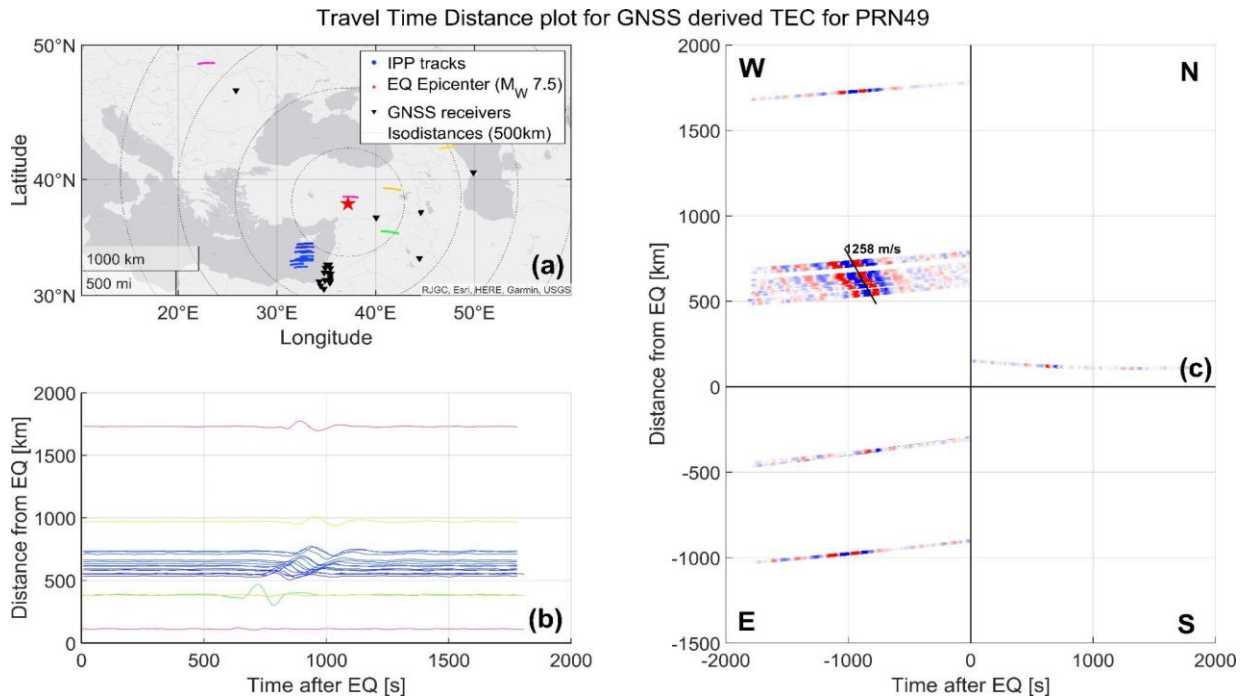
517  
518  
519  
520

521 Thanks to the combination of the two TTDs, we can investigate the waveform and amplitude  
522 along with the propagation velocities for different azimuthal ranges. First, Panel (b) of Figure 10  
523 shows how a narrow azimuthal range presents a large amplitude. If we look at the corresponding  
524 IPP tracks, color-coded as in Panel (b), we can discern which geographical area these azimuths  
525 correspond to. Such waveforms are related to GNSS stations located in Cyprus, and the likely  
526 reasons for such this large amplitude could be the observational geometry (IPPs for PRN17) are  
527 actually situated over the epicenter) and earthquake characteristics (such as fault alignment and  
528 focal mechanism (Astafyeva, 2019; Astafyeva & Heki, 2009). The possible impact of such  
529 effects will be discussed below. The waveform visible in all the Panels (b) resembles the typical  
530 acoustic N shape, corresponding to an initial overpressure half cycle with a steep rise-time and a  
531 slower pressure decay followed by a half cycle of rarefaction (Astafyeva, 2019).

532

533 Panels (b), indicate waves of different nature we know from the literature to be produced by  
534 earthquakes. The first TID type, the co-seismic disturbance produced above the epicenter, is  
535 visible in both the South and West subpanels of Panel (c) of Figure 10 and 11 and in the West  
536 subpanel of Figure 12. Note here that the difference in the TID velocity is easily explained by the  
537 fact that the small distance covered by the first shock acoustic wave makes it difficult to reliably  
538 and accurately identify such waves. Moreover, the near-field TID shows almost no signature for  
539 those stations located North of the epicenter, which was expected due to the adverse geometry of  
540 the wave vector and MFLs. The lack of signatures East of the epicenter in Figure 10 and 9 is  
541 instead due to the scarcity of GNSS data accessible for those regions and as well due to the  
542 adverse observational geometry. A similar reasoning applies to the south panel of Figure 11,  
543 where due to the adverse geometry, no clear signatures are visible even if the mutual orientation  
544 of the wave vector and MFLs is optimal. The few stations that are available showed clear TID  
545 signatures East and West of the epicenter for PRN49 where the mutual orientation of the wave

546 vector and observational link was favorable (See Figure 12). This azimuthal anisotropy is in  
 547 good agreement with previous studies (Zettergren & Sniveley, 2019), which used models and  
 548 measurements to explain such behaviors (Bagiya et al., 2019; Rolland et al., 2013). To sum up,  
 549 the near field TID was defined by a 2-3 minutes period, a maximum amplitude of 1 TECu for  
 550 stations located in Cyprus, and a propagation speed of  $\sim 1.150$  km/s. In addition, such wave was  
 551 detected by PRN 17, 49 and 58, East, South and West of epicenter, with signatures spanning  
 552 from a few kilometers to almost 1000 km away from the epicenter.  
 553



554  
 555 **Figure 12.** (a) Spatial distribution of IPPs and the epicenter location, (b) Travel-time diagram for the  
 556 stations shown in (a) and to be completed. (c) Travel-time diagram for different azimuth for PRN49.  
 557

558 The second type of TIDs is the one produced by propagating seismic waves. The West subpanel  
 559 of Panel (c) in Figure 10 shows a clear signature of such Rayleigh wave-induced TIDs.  
 560 Specifically, such waves propagated at around 3 km/s, and the first signature was visible around  
 561 11 minutes after the earthquake.

562 Since the expected delay is normally 8 to 9 minutes, we can understand the slightly longer delay  
 563 due to the fact that the Rayleigh wave had to propagate from the epicenter to the projection on  
 564 the earth's surface of the first IPP that shows the TID (around 200km, which corresponds to  
 565 around 1 minute). The period of such Rayleigh-induced TIDs is nearly the same as for the near-  
 566 field one, thus around 2.5 minutes. Moreover, in the South quadrant of Panel (c) of Figure 10 it  
 567 seems that two different waves are interacting. Specifically, the first TID signature (the one that  
 568 shows a speed of 1215 m/s) is interpreted as the co-seismic TID propagating from the epicenter,  
 569 while for IPPs further than -500 km, it looks as if a faster wave appeared before the near-field  
 570 one and interacted with it. This pattern could be explained by Rayleigh waves propagating  
 571 through the ground at speeds around three times higher than the co-seismic TID, which  
 572 propagates at the speed of sound if the F-layer. Therefore, the Rayleigh wave overcoming the

573 slower near-field TID can explain the mode splitting at around -500 km in the South quadrant. A  
574 similar behaviour is also visible in the West quadrant of Figure 11, where two TIDs appeared in  
575 the same observation arcs. The first one, with a speed of 3020 m/s, is the Rayleigh wave  
576 signature, while the slower one is the co-seismic one. The arcs showing such signatures are all  
577 further than 600km, which is consistent with Panel (c) of Figure 10, where the two modes  
578 splitting happens around 500 km of distance. This behavior of two modes splitting is typical of  
579 earthquake-induced TIDs, and many examples are available in the literature (see e.g., Astafyeva,  
580 2019).

581

#### 582 **4. Synopsis and conclusions**

583

584 The networks of different instruments (GNSS receivers, ionosondes, CDSS, seismographs)  
585 exploited for this study allowed us to study several aspects of the earthquake-induced various  
586 ionospheric disturbances. The first one to appear, was induced by the shock acoustic wave  
587 excited by the earth's crust movement close to the epicenter. The near-field TIDs parameters are  
588 in accordance with those described by Vesnin et al. (2023), and those seen for other earthquakes  
589 that have been studied in the past (Astafyeva, 2019; Kakinami et al., 2013). Moreover, as  
590 discussed in the results section, this shock acoustic wave -induced TIDs with a clear anisotropy  
591 in the azimuth of propagation, as almost no clear shock acoustic wave related signature is visible  
592 for stations located north of the epicenter. This behavior is again in agreement with models  
593 (Bagiya et al., 2019; Otsuka et al., 2006; Rolland et al., 2013) and instrumental results  
594 (Astafyeva et al., 2009; Kakinami et al., 2013).

595

596 The second type of TID detected is the one related to Rayleigh waves. Thanks to the TEC  
597 hodocrone, we know that such a wave had a speed of around 3 km/s and a period of around 2,5  
598 minutes, a common value for this type of perturbation. As for the near-field TIDs, the Rayleigh  
599 wave shows no clear TID signatures for IPPs North of the epicenter but can instead be traced  
600 further though disturbances seen in ionograms. Note that, as the TIDs produced by earthquakes  
601 are of medium scale, they are seen as distortions in individual ionograms. As shown in Venin et  
602 al. (2023), ionospheric characteristics such as foF2 do not show a clear effect. In earlier literature  
603 (Astafyeva et al., 2009; Galvan et al., 2012, Jin et al., 2015), it was possible to trace different  
604 TID modes in GNSS derived TEC up to almost 2000 km. However, those works analysed the  
605 ionospheric response of more powerful earthquakes, with  $MW > 8$ . This can explain why we did  
606 not see a clear TEC signature at such long distances. This work illustrates the complementarity  
607 of ionosonde and GNSS receiver data, as relatively weak disturbances can still be detected as  
608 multi cusp signatures in ionograms at much larger distances.

609 Another pattern discernible from the GNSS-related figures common for co-seismic TIDs is the  
610 two-mode splitting, which happens around 500 and 600 km away from the epicenter for Figure  
611 10 and 11 respectively. This two modes splitting behavior is typical of earthquake-induced TIDs,  
612 and many examples are available in the literature (Astafyeva et al., 2009; Kakinami et al., 2013).  
613 Finally, using continuous Doppler sounding systems, it was possible to detect infrasound  
614 signatures associated with different types of seismic waves. The infrasound signature associated  
615 with the P and S waves is not discernable in the TEC data or even in the ionograms analysed.  
616 This further illustrates how the use of multiple instruments is required for observing the entire  
617 spectrum of ionospheric disturbances generated by seismic events.

618 It is worth comparing the ionospheric disturbances described here to those detected after the  
619 eruption of the Hunga Tonga volcano in January 2022 (e.g., Chum et al. 2023, Astafyeva et al.,  
620 2022; Themens, et al. 2022, Maletckii & Astafyeva, 2022, Verhulst et al., 2022), as the latter was  
621 the first such eruption in a long time, and the first for which data quality and coverage was  
622 comparable to the earthquake discussed here. After this eruption, TIDs were observed circling  
623 the entire globe multiple times. This is not the case for the earthquake analysed here, although  
624 TID propagation over longer distances is possible for more powerful earthquakes. However, also  
625 the mechanisms for impacting the ionosphere are different between earthquakes and volcanic  
626 eruptions. In the case of the volcanic eruption, the most significant mechanism for influencing  
627 the ionosphere was the Lamb wave, a feature not present in the context of earthquakes. Thus,  
628 although various impulsive events produce signatures in the ionosphere, the nature of their  
629 source is important in determining what type of waves will be detected. Conversely, this  
630 confirms that the details of the observed ionospheric waves can be used to identify the nature of  
631 the earthquake event, as proposed by Sevastano et al. (2017) and Astafyeva (2019).  
632 One aspect of the observations that is clearly similar between events is the anisotropy of the  
633 propagation of ionospheric disturbances produced directly over the source. This was also seen  
634 after the Hunga eruption, as there was significant anisotropy in the TIDs close to the site of the  
635 eruption (Themens et al., 2023). Similar anisotropic propagation was also observed for TIDs  
636 from other sources, for instance in the analysis of Luo et al. (2020) concerning a major meteor  
637 impact. This therefore must be considered a general feature of TIDs excited by impulsive point  
638 sources.

639  
640  
641

#### 642 **Acknowledgments**

643 Part of this work was funded by: a) T-FORS project by European Commission (number SEP-  
644 210818055) and project SAV-23-02 by the Czech Academy of Sciences.

645 Some of the authors were partially funded through the EU projects PITHIA-NRF (Grant nr.  
646 101007599) and T-FORS (Grant nr. 101081835)

647 The contribution of VB was supported by the Hungarian National Research, Development and  
648 Innovation Office and by Bolyai Fellowship (GD, no. BO/00461/21). The ionograms from the  
649 Athens ionosonde were provided by Dr. Anna Belehaki. The authors wish to thank the seismic  
650 data to the ORFEUS (European infrastructure for seismic waveform data), furthermore to the  
651 European Integrated Data Archive (EIDA) and all the EU projects and institutions that supported  
652 them.

653  
654

#### 655 **The datasets analyzed for this study can be found in the:**

656 The SymH and Kp geomagnetic indices are provided by the World Data Center for  
657 Geomagnetism of Kyoto ([http:// wdc. kugi. kyoto-u. ac. jp/ index. html](http://wdc.kugi.kyoto-u.ac.jp/index.html)), while the PC index by  
658 the Arctic and Antarctic Research Institute or Russia and the Technical University of Denmark  
659 (PCI, [https:// pcind ex. org/](https://pcindex.org/)). DSCOVER data are available at National Centers for Environmental  
660 Information of NOAA (<https://www.ngdc.noaa.gov/dscovr/portal/index.html#/>). The ionograms  
661 analysed can be found in the GIRO (<https://giro.uml.edu>) and eSWua <http://www.eswua.ingv.it/>)  
662 repositories. The CDSS data can be found in the archive maintained by IAP

663 <http://datacenter.ufa.cas.cz/>). Seismic data is available in the European Integrated Data Archive  
664 (EIDA) through the following link: <https://www.orfeus-eu.org/data/>. The GNSS database  
665 containing all the RINEX files used for this study can be found at the following link:  
666 <https://doi.org/10.5281/zenodo.7923587>

667  
668

### 669 **Conflicts of Interest:**

670 The authors declare no conflict of interest.

671  
672  
673

### 674 **References**

675

676 Afraimovich, E. L., Perevalova, N. P., Plotnikov, A. V., & Uralov, A. M. (2001). *The shock-acoustic*  
677 *waves generated by earthquakes*. *Annales Geophysicae*, 19(4), 395–409. [https://doi.org/10.5194/angeo-](https://doi.org/10.5194/angeo-19-395-2001)  
678 19-395-2001

679 Afraimovich, E.L., Astafyeva, E.I. & Zhivetiev, I.V. *Solar activity and global electron content*. *Dokl.*  
680 *Earth Sc.* 409, 921–924 (2006). <https://doi.org/10.1134/S1028334X06060195>

681 Astafyeva, E., & Heki, K. (2009). *Dependence of waveform of near-field co-seismic ionospheric*  
682 *disturbances on focal mechanisms*. *LETTER Earth Planets Space* (Vol. 61, pp. 939–943). Retrieved from  
683 [www.eri.u-tokyo.ac.jp/sanchu/SeismoNote/](http://www.eri.u-tokyo.ac.jp/sanchu/SeismoNote/).

684 Astafyeva, E., Heki, K., Kiryushkin, V., Afraimovich, E., & Shalimov, S. (2009). Two-mode long-distance  
685 propagation of co-seismic ionosphere disturbances. *Journal of Geophysical Research: Space Physics*,  
686 114(10). <https://doi.org/10.1029/2008JA013853>

687 Astafyeva, E., Maletkii, B., Miksell, T. D., Munaibari, E., Ravanelli, M., Coisson, P., Manta, F., and  
688 Rolland, L. (2022) *The 15 January 2022 Hunga Tonga Eruption History as Inferred From Ionospheric*  
689 *Observations*, *Geophys. Res. Lett.* 49(10), e2022GL098827, doi:10.1029/2022GL098827  
690 Astafyeva, E. (2019). Ionospheric Detection of Natural Hazards. *Reviews of Geophysics*, 57(4), 1265–1288.  
691 <https://doi.org/10.1029/2019RG000668>

692 Astafyeva, E.I. and Afraimovich, E.L. (2019), *Long-distance traveling ionospheric disturbances caused by*  
693 *the great Sumatra-Andaman earthquake on 26 December 2004*, *Earth Planets and Space*, Vol.58, Issue 8,  
694 1025-1031, DOI10.1186/BF03352607

695 Artru, J, Farges, T and Lognonne, P. (2004), *Acoustic waves generated from seismic surface waves:*  
696 *propagation properties determined from Doppler sounding observations and normal-mode modelling*.  
697 *Geophysical Journal International*, Vol.158, Issue 3, 1067-1077, DOI10.1111/j.1365-246X.2004.02377.x

698 Bagiya, M. S., Sunil, A. S., Rolland, L., Nayak, S., Ponraj, M., Thomas, D., & Ramesh, D. S. (2019).  
699 *Mapping the Impact of Non-Tectonic Forcing mechanisms on GNSS measured Co-seismic Ionospheric*  
700 *Perturbations*. *Scientific Reports*, 9(1). <https://doi.org/10.1038/s41598-019-54354-0>

701 Bass H, Sutherland ELC, Piercy J, Evans L (1984), *Absorption of sound by the atmosphere*, in *Physical*  
702 *Acoustics*, Vol. XVII, Chap. 3., edited by W.P. Mason and R.N. Thurston, 145-232, Academic Press, Inc  
703 Chum, J., F. Hruska, J. Zednik, and J. Lastovicka (2012), Ionospheric disturbances (infrasound waves)  
704 over the Czech Republic excited by the 2011 Tohoku earthquake, *J. Geophys. Res.*, 117, A08319,  
705 doi:10.1029/2012JA017767

706 Chum, J., F.A.M. Bonomi, J. Fišer, M.A. Cabrera, R.G. Ezquer, D. Burešová, J. Laštovička, J. Baše, F.  
707 Hruška, M.G. Molina, J.E.Ise, J.I. Cangemi, and T. Šindelářová (2014), *Propagation of gravity waves and*  
708 *spread F in the low-latitude ionosphere over Tucumán, Argentina, by continuous Doppler sounding: First*  
709 *results*, *J. Geophys. Res.Space Physics*, 119, 6954–6965, doi:10.1002/2014JA020184.

710 Chousianitis, K., Papanikolaou, X., Drakatos, G., & Tselentis, G. -Akis. (2021). NOANET: A  
711 Continuously Operating GNSS Network for Solid-Earth Sciences in Greece. *Seismological Research*  
712 *Letters*, 92(3), 2050–2064. <https://doi.org/10.1785/0220200340>  
713 Chum J., Y.-J. Liu, J. Laštovička, J. Fišer, Z. Mošna, J. Baše, Y.Y. Sun (2016a), Ionospheric signatures of  
714 the April 25, 2015 Nepal earthquake and the relative role of compression and advection for Doppler  
715 sounding of infrasound in the ionosphere, *Earth, Planets, Space*, 68:24, DOI 10.1186/s40623-016-0401-9  
716 Chum, J., M. A. Cabrera, Z. Mošna, M. Fagre, J. Baše, and J. Fišer (2016b), Nonlinear acoustic waves in  
717 the viscous thermosphere and ionosphere above earthquake, *J. Geophys. Res. Space Physics*, 121,  
718 doi:10.1002/2016JA023450.  
719 Chum, J., J.-Y. Liu, K. Podolská, T. Šindelářová (2018a), Infrasound in the ionosphere from earthquakes  
720 and typhoons, *J. Atmos. Sol. Terr. Phys.*, 171, 72-82, doi:/10.1016/j.jastp.2017.07.022  
721 Chum, J., Urbář, J., Laštovička, J., Cabrera, M. A., Liu, J.Y., Bonomi, F., Fagre, M., Fišer, J. & Mošna, Z.  
722 (2018b), Continuous Doppler sounding of the ionosphere during solar flares, *Earth, Planets and Space*,  
723 2018, 70:198, <https://doi.org/10.1186/s40623-018-0976-4>  
724 Chum, J., Podolská, K., Rusz, J., Baše, J., Tedoradze, N. (2021), Statistical investigation of gravity wave  
725 characteristics in the ionosphere. *Earth Planets Space* 73, 60, <https://doi.org/10.1186/s40623-021-01379-3>  
726 Chum J., Šindelářová T., Koucká Knížová P., Podolská K., Rusz J., Baše J., Nakata H., Hosokawa K.,  
727 Danielides M., Schmidt C., Knez L., Liu J-Y., Molina M.G., Fagre M., Katamzi-Joseph Z., Ohya H.,  
728 Omori T., Laštovička J., Obrazová Burešová D., Kouba D., Urbář J., Truhlík V. (2023), Atmospheric and  
729 ionospheric waves induced by the Hunga eruption on 15 January 2022; Doppler sounding and infrasound,  
730 *Geophys. J. Int.* (2023) 233, 1429–1443, <https://doi.org/10.1093/gji/ggac517>  
731 Cicone, A., & Zhou, H. (2021). Numerical analysis for iterative filtering with new efficient  
732 implementations based on FFT. *Numerische Mathematik*, 147(1), 1–28. [https://doi.org/10.1007/s00211-](https://doi.org/10.1007/s00211-020-01165-5)  
733 [020-01165-5](https://doi.org/10.1007/s00211-020-01165-5)  
734 Dal Zilio, L., & Ampuero, J. P. (2023). Earthquake doublet in Turkey and Syria. *Communications Earth*  
735 *& Environment*, 4(1), 71  
736 Danezis, C., Chatzinikos, M., & Kotsakis, C. (2019). LINEAR AND NONLINEAR DEFORMATION  
737 EFFECTS IN THE PERMANENT GNSS NETWORK OF CYPRUS (version 2019).  
738 David A. Galvan, Attila Komjathy, Michael P. Hickey, Philip Stephens, Jonathan Snively, Y. Tony Song,  
739 Mark D. Butala, and Anthony J. Mannucci (2012): “Ionospheric signatures of Tohoku-Oki tsunami of  
740 March 11, 2011: Model comparisons near the epicenter,” *Radio Sci.*, 47(4), RS4003,  
741 doi:10.1029/2012rs005023  
742 Davies K., Watts J., Zacharisen D. (1962), A study of F2-layer effects as observed with a Doppler  
743 technique. *J Geophys Res* 67:2. doi:10.1029/JZ067i002p00601  
744 Dow, J. M., Neilan, R. E., & Rizos, C. (2009). The International GNSS Service in a changing landscape  
745 of Global Navigation Satellite Systems. *Journal of Geodesy*, 83(3), 191–198.  
746 <https://doi.org/10.1007/s00190-008-0300-3>  
747 Drob, D. P., et al. (2015), An update to the Horizontal Wind Model (HWM): The quiet time  
748 thermosphere, *Earth Space Sci.*, 2, 301–319, doi:10.1002/2014EA000089.  
749 Eric Calais and J. Bernard Minster (1995): “GPS detection of ionospheric perturbations following the  
750 January 17, 1994, Northridge Earthquake,” *Geophys. Res. Lett.* 22(9), 1045–1048,  
751 doi:10.1029/95gl00168.  
752 Ducic, V., Artru, J., & Lognonné, P. (2003). Ionospheric remote sensing of the Denali Earthquake  
753 Rayleigh surface waves. *Geophysical Research Letters*, 30(18). <https://doi.org/10.1029/2003GL017812>  
754 Georges, T.M., 1973. Infrasound from convective storms: examining the evidence. *Rev. Geophys. Space*  
755 *Phys.* 11, 571–594.  
756 Galvan, D. A., Komjathy, A., Hickey, M. P., Stephens, P., Snively, J., Song, Y. T., Butala, M. D., and  
757 Mannucci, A. J. (2012) *Ionospheric signatures of Tohoku-Oki tsunami of March 11, 2011: Model*  
758 *comparisons near the epicenter*, *Radio Sci.* 47, RS4003, doi:10.1029/2012rs005023.

759 Heki, K., & Ping, J. (2005). Directivity and apparent velocity of the co-seismic ionospheric disturbances  
760 observed with a dense GPS array. *Earth and Planetary Science Letters*, 236(3), 845–855.  
761 <https://doi.org/10.1016/j.epsl.2005.06.010>

762 István Bondár and Dmitry Storck (2011): Improved location procedures at the International  
763 Seismological Centre, *Geophys. J. Int.* 186(3), 1220–1244, doi:10.1111/j.1365-246X.2011.05107.x.

764 Jacobs JA, Watanabe T (1966) Doppler frequency changes in radio waves propagating through a moving  
765 ionosphere. *Radio Science* 1(3):257–264

766 Jin, S., Occhipinti, G., and Jin., R. (2015) GNSS ionospheric seismology: Recent observation evidences  
767 and characteristics, *Earth-Sci. Rev.* 147, 54–64, doi:10.1016/j.earscirev.2015.05.003.

768 Kakinami, Y., Kamogawa, M., Watanabe, S., Odaka, M., Mogi, T., Liu, J. Y., et al. (2013). Ionospheric  
769 ripples excited by superimposed wave fronts associated with Rayleigh waves in the thermosphere.  
770 *Journal of Geophysical Research: Space Physics*, 118(2), 905–911. <https://doi.org/10.1002/jgra.50099>

771 Kauristie, K., Morschhauser, A., Olsen, N., Finlay, C. C., McPherron, R. L., Gjerloev, J. W., &  
772 Opgenoorth, H. J. (2017). On the usage of geomagnetic indices for data selection in internal field  
773 modelling. *Space Science Reviews*, 206, 61-90.

774 Kemal Önder Çetin, Makbule İlgaç, Gizem Can, and Elife Çakır (2023): Preliminary Reconnaissance  
775 Report on February 6, 2023, Pazarcık  $M_w=7.7$  and Elbistan  $M_w=7.6$  Kahramanmaraş-Türkiye  
776 Earthquakes, Report no: METU/EERC 2023-01, Middle East Technical University – Earthquake  
777 Engineering Research Center.

778 Kenneth Davies and Donald M. Baker (1965): “Ionospheric effects observed around the time of the  
779 Alaskan earthquake of March 28, 1964,” *J. Geophys. Res.* 70(9), 2251–2253,  
780 doi:10.1029/jz070i009p02251.

781 Kikuchi T, Chum J., Tomizawa I, Kumiko K. K K, Hosokawa K, Ebihara Y, Hozumi K, Supnithi P  
782 (2021), Penetration of the electric fields of the geomagnetic sudden commencement over the globe as  
783 observed with the HF Doppler sounders and magnetometers, *Earth, Planets and Space*, 73:10,  
784 <https://doi.org/10.1186/s40623-020-01350-8>

785 Kikuchi T., Araki T., Hashimoto K. K., Ebihara Y., Tanaka T., Nishimura Y., Vichare G., Sinha A. K.,  
786 Chum J., Hosokawa K., Tomizawa I., Tanaka Y., Kadokura A. (2022), Instantaneous Achievement of the  
787 Hall and Pedersen–Cowling Current Circuits in Northern and Southern Hemispheres During the  
788 Geomagnetic Sudden Commencement on 12 May 2021, *Front. Astron. Space Sci.* 9: 879314,  
789 <https://doi.org/10.3389/fspas.2022.879314>

790 Komjathy, A., Yang, Y. M., Meng, X., Verkhoglyadova, O., Mannucci, A. J., & Langley, R. B. (2016).  
791 Review and perspectives: Understanding natural-hazards-generated ionospheric perturbations using GPS  
792 measurements and coupled modeling. *Radio Science*, 51(7), 951–961.  
793 <https://doi.org/10.1002/2015RS005910>

794 Kosuke Heki (2021): “Ionospheric Disturbances Related to Earthquakes,” in: Chaosong Huang and Gang  
795 Lu (eds.) *Space Physics and Aeronomy, Volume 3, Ionosphere Dynamics and Applications* (chapter 21),  
796 John Wiley & Sons, NJ USA, International Seismological Centre (2023), On-line Bulletin,  
797 doi:/10.31905/D808B830.

798 Laštovička, J., and J. Chum (2017) A review of results of the international ionospheric Doppler sounder  
799 network, *Adv. Space Res.*, 60, 1629-1643, <http://dx.doi.org/10.1016/j.asr.2017.01.032>

800 Leonard R.S. and R.A. Barnes, Jr. (1965): “Observation of ionospheric disturbances following the Alaska  
801 earthquake,”. *Geophys. Res.* 70(5), 1250–1253, doi:10.1029/jz070i005p01250.

802 Li, H., Wang, C., & Kan, J. R. (2011). Contribution of the partial ring current to the SYMH index during  
803 magnetic storms. *Journal of Geophysical Research*, 116(A11), A11222.

804 Liu, J.Y. , Y. B. Tsai, S. W. Chen, C. P. Lee, Y. C. Chen, H. Y. Yen, W. Y. Chang, and C. Liu (2006):  
805 “Giant ionospheric disturbances excited by the M9.3 Sumatra earthquake of 26 December 2004,”  
806 *Geophys. Res. Lett.* 33(2), L02103, doi:10.1029/2005gl023963

807 Liu, J.Y., Yang, S.S., Rajesh, P.K., Sun Y.Y., Chum, J., Pan, C.J., Chu, Y.H., Chao, C.K. and Chang L.C.  
808 (2019), Ionospheric response to the 21 May 2012 annular solar eclipse over Taiwan, *Journal of*  
809 *Geophysical Research: Space Physics*, 124, 3623–3636. <https://doi.org/10.1029/2018JA025928>

810 Luca Dal Zilio and Jean-Paul Ampuero (2023): “Earthquake doublet in Turkey and Syria,” *Commun.*  
811 *Earth Environ.* 4, 71, doi:10.1038/s43247-023-00747

812 Lucie M. Rolland, Philippe Lognonné, and Hiroshi Munekane (2011): “Detection and modeling of  
813 Rayleigh wave induced patterns in the ionosphere,” *J. Geophys. Res.*, 11, A05320,  
814 doi:10.1029/2010AJ016060.

815 Madonia, P., Bonaccorso, A., Bonforte, A., Buonocunto, C., Cannata, A., Carleo, L., et al. (2023).  
816 Propagation of Perturbations in the Lower and Upper Atmosphere over the Central Mediterranean, Driven  
817 by the 15 January 2022 Hunga Tonga-Hunga Ha’apai Volcano Explosion. *Atmosphere*, 14(1), 65.  
818 <https://doi.org/10.3390/atmos14010065>

819 Michelini, A., Margheriti, L., Cattaneo, M., Cecere, G., D’Anna, G., Delladio, A., et al. (2016). The  
820 Italian National Seismic Network and the earthquake and tsunami monitoring and surveillance systems.  
821 *Advances in Geosciences*, 43, 31–38. <https://doi.org/10.5194/adgeo-43-31-2016>

822 NOAA Space Weather Prediction Center (2016): Deep Space Climate Observatory (DSCOVR). NOAA  
823 National Centers for Environmental Information. Dataset. <http://doi.org/10.7289/V51Z42F7>

824 Maletckii, B. and Astafyeva, E. (2022) *Near-Real-Time Analysis of the Ionospheric Response to the 15*  
825 *January 2022 Hunga Tonga-Hunga Ha’apai Volcanic Eruption*, *J. Geophys. Res.* 127(10),  
826 e2022JA030735, doi:10.1029/2022JA030735.

827 Mannucci, A. J., Wilson, B. D., Yuan, D. N., Ho, C. H., Lindqwister, U. J., & Runge, T. F. (1998). A  
828 global mapping technique for GPS-derived ionospheric total electron content measurements. *Radio*  
829 *Science*, 33(3), 565–582. <https://doi.org/10.1029/97RS02707>

830 Maruyama, T., Tsugawa, T., Kato, H., Saito, A., Otsuka, Y., and Nishioka, M.: Ionospheric multiple  
831 stratifications and irregularities induced by the 2011 off the Pacific coast of Tohoku Earthquake, *Earth*  
832 *Planets Space*, 63, 65, <https://doi.org/10.5047/eps.2011.06.008>, (2011)

833 Maruyama, T., T. Tsugawa, H. Kato, M. Ishii, and M. Nishioka, Rayleigh wave signature in ionograms  
834 induced by strong earthquakes, *J. Geophys. Res.*, 117, A08306, doi:10.1029/2012JA017952, (2012)

835 Maruyama, T., and H. Shinagawa, Infrasonic sounds excited by seismic waves of the 2011 Tohoku-oki  
836 earthquake as visualized in ionograms, *J. Geophys. Res. Space Physics*, 119, 4094–4108,  
837 doi:10.1002/2013JA019707, (2014)

838 Nava, B., Coisson, P., & Radicella, S. M. (2008). A new version of the NeQuick ionosphere electron  
839 density model. *Journal of Atmospheric and Solar-Terrestrial Physics*, 70(15), 1856–1862.  
840 <https://doi.org/10.1016/j.jastp.2008.01.015>

841 Otsuka, Y., Kotake, N., Tsugawa, T., Shiokawa, K., Ogawa, T., Saito, S., et al. (2006). *GPS detection of*  
842 *total electron content variations over Indonesia and Thailand following the 26 December 2004*  
843 *earthquake*. *Earth Planets Space* (Vol. 58, pp. 159–165).

844 Ouml, & Yildirim, M. (2011). A comparative analysis of the virtual reference stations (VRS). *Scientific*  
845 *Research and Essays*, 6(27), 5726–5733. <https://doi.org/10.5897/SRE11.786>

846 Perevalova, V, V.A. Sankov, E.I. Astafyeva, and A.S. Zhupityaeva (2014): “Treshold magnitude for  
847 ionospheric TEC response to earthquakes,” *J. Atmos. Sol. Terr. Phys.* 108, 77–90,  
848 doi:10.1016/j.jastp.2013.12.014.

849 Philippe Lognonné, Juliette Artru, Raphael Garcia, François Crespon, Vesna Ducic, Eric Jeansou,  
850 Giovanni Occhipinti, Jérôme Helbert, Guilhelm Moreaux, and Pierre-Emmanuel Godet (2006): “Ground-  
851 based GPS imaging of ionospheric post-seismic signal,” *Planet. Space Sci.* 54(5), 528–540,  
852 doi:10.1016/j.pss.2005.10.021.

853 Rolland, L., Lognonné, P., Munekane, H. M., Rolland, L. M., & Munekane, H. (2011). Detection and  
854 modeling of Rayleigh wave induced patterns in the ionosphere. *Journal of Geophysical Research Space*  
855 *Physics*, 116(A5), 5320. <https://doi.org/10.1029/2010JA016060>

856 Rolland, L. M., Vergnolle, M., Nocquet, J. M., Sladen, A., Dessa, J. X., Tavakoli, F., et al. (2013).  
857 Discriminating the tectonic and non-tectonic contributions in the ionospheric signature of the 2011,  
858 Mw7.1, dip-slip Van earthquake, Eastern Turkey. *Geophysical Research Letters*, 40(11), 2518–2522.  
859 <https://doi.org/10.1002/grl.50544>

860 Sevastano, G., Komjathy, A., Verkhoglyandova, O. Mazzoni, A., Crespi, M., Wei, Y. et al. (2017) Real-  
861 Time Detection of Tsunami Ionospheric Disturbances with a Stand-Alone GNSS Receiver: A Preliminary  
862 Feasibility Demonstration, *Sci. Rep.* 7, 46607, doi:10.1038/srep46607.  
863 Sindelarova T., Mosna Z., Chum J., Kouba D., Base J., Liu J.Y., and Katamzi-Joseph Z. (2018), Solar  
864 eclipse effects in the ionosphere observed by continuous Doppler sounding, *Adv. Space Res.*, 62, 785-  
865 800, <http://dx.doi.org/10.1016/j.asr.2018.05.029>  
866 Stauning P (2013) The polar cap index: a critical review of methods and a new approach. *J Geophys Res*  
867 *Space Phys* 118(8):5021–5038  
868 Strollo, A., Cambaz, D., Clinton, J., Danecek, P., Evangelidis, C. P., Marmureanu, A., & Triantafyllis, N.  
869 (2021). EIDA: The European integrated data archive and service infrastructure within ORFEUS.  
870 *Seismological Society of America*, 92(3), 1788-1795.  
871 Takashi Maruyama, Kamil Yusupov, and Adel Akchurin (2016a): “Interpretation of deformed ionograms  
872 induced by vertical ground motion of seismic Rayleigh waves and infrasound in the thermosphere” *Ann.*  
873 *Geophys.* 34(2), 271–278, doi:10.5194/angeo-34-271-2016.  
874 Takashi Maruyama, Kamil Yusupov, and Adel Akchurin (2016b): “Ionosonde tracking of infrasound  
875 wavefronts in the thermosphere launched by seismic waves after the 2010 M8.8 Chile earthquake,” *J.*  
876 *Geophys. Res.* 121(3), 2683–2692, doi:10.1002/2015ja022260.  
877 Torres, J. A., Altamimi, Z., Boucher, C., Brockmann, E., Bruyninx, C., Caporali, A., et al. (2009). Status  
878 of the European Reference Frame (EUREF). In M. G. Sideris (Ed.), *Observing our Changing Earth* (pp.  
879 47–56). Berlin, Heidelberg: Springer. [https://doi.org/10.1007/978-3-540-85426-5\\_6](https://doi.org/10.1007/978-3-540-85426-5_6)  
880 Themens, D. R., Watson, C., Žagar, N., Vasylkevych, S., Elvidge, S., McCaffrey, A., Prikryl, P., Reid, B.,  
881 Wood, A., and Jayachandran, P. T. (2022) Global Propagation of Ionospheric Disturbances Associated  
882 With the 2022 Tonga Volcanic Eruption, *Geophys. Res. Lett.* 49(7), e2022GL098158,  
883 doi:10.1029/2022GL098158.  
884 US Geological Survey (2023): Event page of the M7.8 - Pazarcik earthquake, Kahramanmaras earthquake  
885 sequence, <https://earthquake.usgs.gov/earthquakes/eventpage/us6000jllz/executive>.  
886 Vanlommel, P. (2018). Solar-Terrestrial Centre of Excellence (STCE) Newsletter, issue 17 Feb 2023.  
887 Available online at <https://www.stce.be/newsletter/>.  
888 Verhulst, T. G. W., Altadill, D., Barta, V., Belehaki, A., Burešová, D., Cesaroni, C., et al. (2022). Multi-  
889 instrument detection in Europe of ionospheric disturbances caused by the 15 January 2022 eruption of the  
890 Hunga volcano. *Journal of Space Weather and Space Climate*, 12, 35.  
891 <https://doi.org/10.1051/swsc/2022032>  
892 Vesnin A, Yasyukevich Y, Perevalova N, Şentürk E. Ionospheric Response to the 6 February 2023  
893 Turkey–Syria Earthquake. *Remote Sensing*. 2023; 15(9):2336. <https://doi.org/10.3390/rs15092336>  
894 Watada S, Kunugi T, Hirata K, Sugioka H, Nishida K, Sekiguchi S, Oikawa J, Tsuji Y, Kanamori H  
895 (2006) Atmospheric pressure change associated with the 2003 Tokachi-Oki earthquake. *Geophys Res Lett*  
896 33, L24306. doi:10.1029/2006GL027967  
897 Xing Meng, Panagiotis Vergados, Attila Komjathy, and Olga Verkhoglyadova (2019): “Upper  
898 Atmospheric Responses to Surface Disturbances: An Observational Perspective,” *Radio Sci.* 54(11),  
899 1076–1098, doi:10.1029/2019rs006858.  
900 Zettergren M.D. and J.B. Snively (2019): “Latitude and Longitude Dependence of Ionospheric TEC and  
901 Magnetic Perturbations From Infrasonic-Acoustic Waves Generated by Strong Seismic Events,”  
902 *Geophys. Res. Lett.* 46, 1132–1140, doi:10.1029/2018GL081569.  
903